Towards understanding polar heat transport enhancement in sub-glacial oceans on icy moons

Robert Hartmann[1], Richard J. A. M. Stevens[1], Detlef Lohse[1], and Roberto Verzicco[2]

[1]University of Twente
[2]Universita' di Roma Tor Vergata

August 4, 2023

Abstract

The interior oceans of several icy moons are considered as "moderately rotating". Observations suggest a larger heat transport around the poles than at the equator. Rotating Rayleigh-Bénard convection (RRBC) in planar configuration is known to show an enhanced heat transport compared to the non-rotating case for such "moderate" rotation. We investigate the potential for such a (polar) heat transport enhancement in these sub-glacial oceans by direct numerical simulations of RRBC in spherical geometry for Ra=10^6 and 0.7[?]Pr[?]4.38. We find an enhancement up to 28% in the "polar tangent cylinder", which is globally compensated by a reduced heat transport at low latitudes. As a result, the polar heat transport can exceed the equatorial by up to 50%. The enhancement is mostly insensitive to different radial gravity profiles, but decreases for thinner shells. In general, polar heat transport and its enhancement in spherical RRBC follow the same principles as in planar RRBC.

Towards understanding polar heat transport enhancement in sub-glacial oceans on icy moons

Robert Hartmann[1], **Richard J. A. M. Stevens**[1], **Detlef Lohse**[1,2], **and Roberto Verzicco**[1,3,4]

[1]Physics of Fluids Group and Twente Max Planck Center, J.M. Burgers Center for Fluid Dynamics, University of Twente, 7500 AE Enschede, The Netherlands
[2]Max Planck Institute for Dynamics and Self-Organisation, 37077 Göttingen, Germany
[3]Dipartimento di Ingegneria Industriale, University of Rome 'Tor Vergata', 00133 Rome, Italy
[4]Gran Sasso Science Institute, 67100 L'Aquila, Italy

Key Points:

- The polar heat transport in spherical rotating Rayleigh-Bénard convection experiences an enhancement by rotation.
- The influence of rotation differs at low latitudes: the heat flux is reduced and compensates the polar enhancement on the global average.
- Enhanced polar heat transport due to Ekman pumping through axial vortices could explain various phenomena on icy moons.

Corresponding author: Robert Hartmann, r.hartmann@utwente.nl

Abstract

The interior oceans of several icy moons are considered as "moderately rotating". Observations suggest a larger heat transport around the poles than at the equator. Rotating Rayleigh-Bénard convection (RRBC) in planar configuration is known to show an enhanced heat transport compared to the non-rotating case for such "moderate" rotation. We investigate the potential for such a (polar) heat transport enhancement in these sub-glacial oceans by direct numerical simulations of RRBC in spherical geometry for $Ra = 10^6$ and $0.7 \leq Pr \leq 4.38$. We find an enhancement up to 28% in the "polar tangent cylinder", which is globally compensated by a reduced heat transport at low latitudes. As a result, the polar heat transport can exceed the equatorial by up to 50%. The enhancement is mostly insensitive to different radial gravity profiles, but decreases for thinner shells. In general, polar heat transport and its enhancement in spherical RRBC follow the same principles as in planar RRBC.

Plain Language Summary

The icy moons of Jupiter and Saturn like e.g., Europa, Titan, or Enceladus are believed to have a water ocean beneath their ice crust. Several of them show phenomena in their polar regions like active geysers or a thinner crust than at the equator, all of which might be related to a larger heat transport around the poles from the underlying ocean. We simulate the flow dynamics and currents in these sub-glacial ocean by high-fidelity simulations, though still at less extreme parameters than in reality, to study the heat transport and provide a possible explanation of such a "polar heat transport enhancement". We find that the heat transport around the poles can be up to 50% larger than around the equator, and that the believed properties of the icy moons and their oceans would allow polar heat transport enhancement. Therefore, our results may help to improve the understanding of ocean currents and latitudinal variations in the oceanic heat transport and crustal thickness on icy moons.

1 Introduction

In the common understanding, most icy satellites in the solar system, e.g., the Jovian and Saturnian moons Europa, Ganymede, Titan, and Enceladus, contain a global ocean layer beneath their ice crust (e.g., Nimmo & Pappalardo, 2016), which gained a lot of interest in terms of habitable environments (e.g., Chyba & Hand, 2005; Vance et al., 2018). In order to asses their habitability, it is crucial to understand their flow dynamics. On Enceladus, for instance, eruptions from fault systems at the south pole (see, e.g., Nimmo & Pappalardo, 2016) suggest a strong polar anomaly of enhanced heat transport. Furthermore, the crustal thickness counterintuitively decreases from the equator towards the poles (e.g., Beuthe et al., 2016; Čadek et al., 2019; Hemingway & Mittal, 2019; Kang, 2022; Kang & Jansen, 2022), which suggests a large-scale latitudinal variation of the heat released from the sub-glacial ocean (Kihoulou et al., 2023). In this study, we investigate the dynamics inside and the heat transport out of these oceans by direct numerical simulations (DNSs) of rotating Rayleigh-Bénard convection (RRBC) in spherical geometry. Therewith, we aim to provide a possible explanation for the origin of the polar enhancement of the heat transport on icy moons.

The canonical system of RRBC in planar configuration has been extensively studied experimentally and numerically (see, e.g., the reviews by Kunnen, 2021; Ecke & Shishkina, 2023; Stevens et al., 2013; Plumley & Julien, 2019, and Refs. therein). Its dynamical behavior is fully controlled by three dimensionless parameters: the Prandtl number Pr describing the fluid properties, the Rayleigh number Ra setting the strength of thermal driving, and the inverse Rossby number Ro^{-1} as a measure for the importance of rotation relative to buoyancy (full definitions in Sec. 2). The influence of rotation can alternatively be parameterized by the Ekman number $Ek = Ro\sqrt{Pr/Ra}$. Several flow regimes and

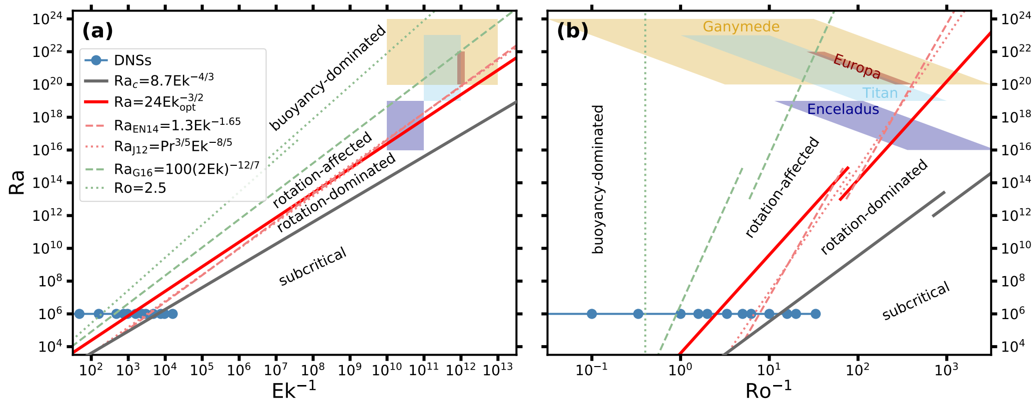

Figure 1. Regime diagram of (planar) RRBC in the parameter space of **(a)** Ra and Ek^{-1} and **(b)** Ra and Ro^{-1} (after Soderlund (2019), see also Kunnen (2021)): The solid gray line denotes the critical Rayleigh number Ra_c for the onset of convection (Chandrasekhar, 1961). The solid red line depicts the transition between the rotation-dominated and the rotation-affected regimes for based on boundary layer crossing and heat transport maximum per fixed Ra for $Pr > 1$ fluids (Yang et al., 2020). Dashed and dotted light red lines are alternative estimates for this transition by Ecke and Niemela (2014) and Julien, Knobloch, et al. (2012), respectively. The dashed and dotted green lines represent the transition between the rotation-affected and the buoyancy-dominated regimes based on Gastine et al. (2016) and for a cylinder with diameter-to-height ratio 1 (Weiss et al., 2010), respectively. The blue circles mark the simulations of spherical RRBC in this study ($Pr = 4.38$). The shaded areas show the predicted parameter range for several icy moons ($10 \leq Pr \leq 13$) as given in (Soderlund, 2019). Line offsets symbolize the Pr dependence of any transition between $Pr = 4.38$ like in our simulations and $Pr = 13$ like the upper bound for the icy moons.

flow states were discovered and studied over the past decades. The three major regimes based on the trend of heat transport with variying rotation are (i) the *buoyancy-dominated* regime at relatively slow rotation, where heat transport and flow dynamics remain unaffected compared to the non-rotating case, (ii) the transitional *rotation-affected* regime, where intermediate or moderate rotation starts to alter the flow, and (iii) the *rotation-dominated* regime for rapid rotation, where the heat transport steeply decreases with increasing rotation that impedes vertical motion (Proudman, 1916; Taylor, 1917), see e.g., Kunnen (2021) and Ecke and Shishkina (2023). Both rotation-affected and rotation-dominated regimes show a broad variety of sub-regimes or flow states, all of which are characterized by columnar vortical structures aligned with the rotation axis (e.g., Julien et al., 1996; Sprague et al., 2006; Stevens et al., 2009; Julien, Rubio, et al., 2012; Stellmach et al., 2014; Cheng et al., 2015; Aguirre Guzmán et al., 2020). Due to the huge variety of flow states, there exist various estimates for the boundaries of the above regimes in the literature (see Kunnen (2021) for a detailed overview) - most of them based on RRBC data in the classical planar configuration. The most common ones are summarized Fig. 1.

An important peculiarity of planar RRBC with $Pr > 1$ is that Ekman pumping through vertically coherent vortices enhances the heat transport in the rotation-affected regime to exceed its non-rotating value (e.g., Rossby, 1969; Kunnen et al., 2006; Zhong et al., 2009; Stevens et al., 2013). For not too large Ra, the enhancing effect is most efficient when thermal and kinetic boundary layers have approximately the same thickness (Stevens et al., 2010; Yang et al., 2020). This creates a heat transport maximum (per fixed Ra) that follows $Ra \propto Ek^{-3/2}$ (Fig. 1, red line; King et al., 2012; Yang et al., 2020). For very turbulent flows, the maximum diverges towards weaker rotation (Yang et al., 2020).

Based on the estimated parameter ranges for Europa, Ganymede, Titan, and Enceladus by Soderlund (2019), their sub-glacial oceans most likely are in the rotation-affected regime (see Fig. 1). Given that the water of these oceans has $Pr \in [10, 13]$ (Soderlund, 2019), they arguably have the potential for heat transport enhancement - at least around the poles, where buoyancy is mostly aligned with the rotation axis as it is in planar RRBC. Evidence of such a polar heat transport enhancement spherical RRBC are present in several studies (Soderlund, 2019; Amit et al., 2020; Bire et al., 2022). We therefore distinguish between two types of heat transport enhancement: (i) enhancement above the non-rotating heat transport in a specific region is considered as *polar/global/... enhancement*, whereas (ii) a larger heat transport at the poles than at the equator is referred to as *latitudinal enhancement*. Since most simulations of spherical RRBC are conducted for $Pr = 1$ (e.g., Soderlund et al., 2012; Gastine et al., 2016; Wang et al., 2021) and all studies on rotation-induced heat transport enhancement focus on planar RRBC (e.g., Stevens et al., 2009, 2010; Weiss et al., 2016; Yang et al., 2020), we aim to bridge this gap and elucidate the potential of spherical RRBC to show polar and/or global heat transport enhancement. Therefore, we set $Pr = 4.38$ as in many simulations and experiments of planar RRBC and cover the entire range of regimes (Fig. 1).

In the following, we introduce spherical RRBC, its control parameters, and our numerical method (Sec. 2). Then, latitudinal variations of the heat transport are analyzed and linked to the predominant structures in the flow (Sec. 3). Subsequently, we discuss the importance of $Pr > 1$ by a direct comparison with $Pr \leq 1$ (Sec. 4), the influence of the shell thickness, i.e., the ocean depth (Sec. 5), the sensitivity to different radial gravity profiles (Sec. 6), and the relevance of the ratio between thermal and kinetic boundary layers for heat transport enhancement in spherical RRBC (Sec. 7). The letter ends with conclusions (Sec. 8).

2 Dynamical equations and numerical method

Spherical RRBC describes the dynamics of a fluid in a spherical shell confined by a hot inner and a cold outer sphere, rotating around a polar axis (Fig. 2(b)) (e.g., Roberts, 1968; Busse, 1970, 1983; Aurnou et al., 2015). The geometry of the system is determined by the inner and outer radii r_i and r_o, defining the shell thickness $H = r_o - r_i$ expressed by the radius ratio $\eta = r_i/r_o$. The dynamics are controlled by the three dimensionless parameters Pr, Ra, and Ro^{-1}, defined as:

$$Pr = \frac{\nu}{\kappa} \ , \ Ra = \frac{\alpha g_0 \Delta T H^3}{\nu \kappa} \ , \ Ro^{-1} = \frac{2\Omega H}{\sqrt{\alpha g_0 \Delta T H}} \ . \tag{1}$$

Therein, ν is the kinematic viscosity, κ the thermal diffusivity, α the isobaric thermal expansion coefficient, g_0 the reference gravitational acceleration at the outer sphere, ΔT the temperature difference between inner and outer sphere, and Ω the angular rotation rate, respectively. Under Oberbeck-Boussinesq approximation, the system is governed by the continuity, Navier-Stokes and temperature convection-diffusion equations, which are given in dimensionless form as:

$$\nabla \cdot \vec{u} = 0 \ , \tag{2}$$

$$\frac{\mathrm{d}\vec{u}}{\mathrm{d}t} = -\nabla P + \sqrt{\frac{Pr}{Ra}} \nabla^2 \vec{u} + \Theta \frac{g(r)}{g_0} \vec{e}_r - \frac{1}{Ro} \vec{e}_z \times \vec{u} \ , \tag{3}$$

$$\frac{\mathrm{d}\Theta}{\mathrm{d}t} = \frac{1}{\sqrt{Pr\, Ra}} \nabla^2 \Theta \ . \tag{4}$$

Therein, $\vec{u}$, P, and Θ denote the normalized velocity, pressure, and temperature fields, respectively. $\mathrm{d}/\mathrm{d}t$ denotes the full, so-called material derivative. $g(r) = g_0 \, (r/r_o)^\gamma$ accounts for radial variations in the gravity profile. The equations are normalized by H and the free-fall velocity $U_0 = \sqrt{\alpha g_0 \Delta T H}$. The temperature is normalized as $\Theta = \frac{T - T_{\mathrm{top}}}{\Delta T} \in [0, 1]$. The pressure field P is reduced by the hydrostatic balance and centrifugal contributions. We consider Coriolis forcing from constant rotation around the polar axis, but neglect centrifugal contributions on buoyancy. Isothermal and no-slip boundary conditions are imposed at the hot inner ($\Theta = 1$) and the cold outer ($\Theta = 0$) spheres.

In this study we conduct direct numerical simulations (DNSs) for $Ra = 10^6$ at $Pr =$ 4.38, 1 and 0.7 while varying the radius ratio η and gravity profile $g(r)$. The DNSs solve the governing equations (Eqs. 2-4) by a central second-order accurate finite-difference scheme based on a staggered grid discretization in spherical coordinates (Santelli et al., 2020), which has been rigorously validated in subsequent studies (Wang et al., 2021, 2022). The computational grid is uniformly spaced in the longitudinal and latitudinal directions, while the grid points in the radial direction are clustered towards the inner and outer spheres. This ensures an appropriate resolution of the Kolmogorov scales in the bulk, as well as of the boundary layers (Shishkina et al., 2010). A summary of grid sizes and numerical parameters can be found in the Supporting Information (Text S1, Tabs. S1-S3).

3 Polar heat transport enhancement

We begin our investigation on a rather thick shell of $\eta = 0.6$ with a constant gravity $g(r) = g_0$. The dimensionless heat transport is given by the Nusselt number Nu. We first consider Nu on the outer sphere as a function of the latitude φ:

$$Nu_{r_o}(|\varphi|) = -\frac{1}{\eta}\partial_r \left.\langle\Theta\rangle_{t,\vartheta,\pm\varphi}\right|_{r_o} \quad . \tag{5}$$

Therein $\langle\cdot\rangle_{t,\vartheta,\pm\varphi}$ indicates averaging in time, longitude, and latitudinal symmetry around the equator. For no and slow rotation ($Ro^{-1} \leq 0.3$), the heat transport is expectably uniform over φ (Fig. 2(a)). Accordingly, the flow is dominated by radial buoyant plumes (Fig. 2(c)), which can organize in a persistent large-scale circulation pattern. Such large-scale circulations are well known from other non-rotating geometries, e.g., RBC in cylindrical containers (e.g., Ahlers et al., 2009, and Refs. therein), 2D RBC (e.g., van der Poel et al., 2013, and Refs. therein), or extremely wide domains (Stevens et al., 2018). However, without rotation, the heat transport ideally is radially symmetric, defining a reference value $Nu_0 = \langle Nu_{r_o}\rangle_\varphi\,(Ro^{-1} = 0)$ (Fig. 2(a), horizontal dashed line).

At intermediate rotation rates ($1 \leq Ro^{-1} \leq 5$), the heat transport is reduced towards the equator and enhanced towards the poles compared to the non-rotating reference (Fig. 2(a)). Taylor columns aligned with the rotation axis form in the flow (Fig. 2(d)) and alter the heat transport. Their vortical motion impedes the radial heat transport around the equator and leads to the formation of sheet-like thermal plumes around the columnar structures (similar to Soderlund et al., 2012; Aurnou et al., 2015). On the contrary, the Taylor columns support the radial heat transport around the poles by Ekman pumping through their interior (in presence of no-slip boundary conditions, e.g., Stellmach et al. (2014)). For $\eta = 0.6$, the polar tangent cylinder, i.e., the cylinder around the inner sphere aligned with the polar axis, intersects with the outer sphere at latitude $|\varphi_{\mathrm{tc}}| = 53.13°$. We use $|\varphi_{\mathrm{tc}}|$ to distinguish between the "polar region" ($|\varphi_{\mathrm{tc}}| < |\varphi| < 90°$), in which ideal axial Taylor columns connect the hot inner sphere with cold outer sphere, and the "low latitude region" ($|\varphi_{\mathrm{tc}}| > |\varphi| > 0°$), in which axial Taylor columns connect the Northern and Southern hemispheres of the outer sphere (Fig. 2(b)). For $1 \leq Ro^{-1} \leq 5$, $|\varphi_{\mathrm{tc}}|$ clearly correlates with the transition from reduced to enhanced heat transport ($Nu_{r_o}(|\varphi_{\mathrm{tc}}|) \approx Nu_0$). The rather smooth trend of $Nu_{r_o}(|\varphi|)$ across $|\varphi_{\mathrm{tc}}|$ however suggests that the inclination between buoyancy (radial) and rotation (axial) additionally influences the enhancement with latitude.

For rapid rotation ($Ro^{-1} \geq 10$), the latitudinal trend in the heat transport is inverted (Fig. 2(a)). At high latitudes, the heat transport quickly decreases with increasing Ro^{-1} down to $Nu_{r_o} = 1$. Towards the equator, the heat transport first increases slightly (compared to the reduction at intermediate rotation), before it also decreases with increasing Ro^{-1}. With increasing rotation the fluid motion is suppressed in the axial direction and

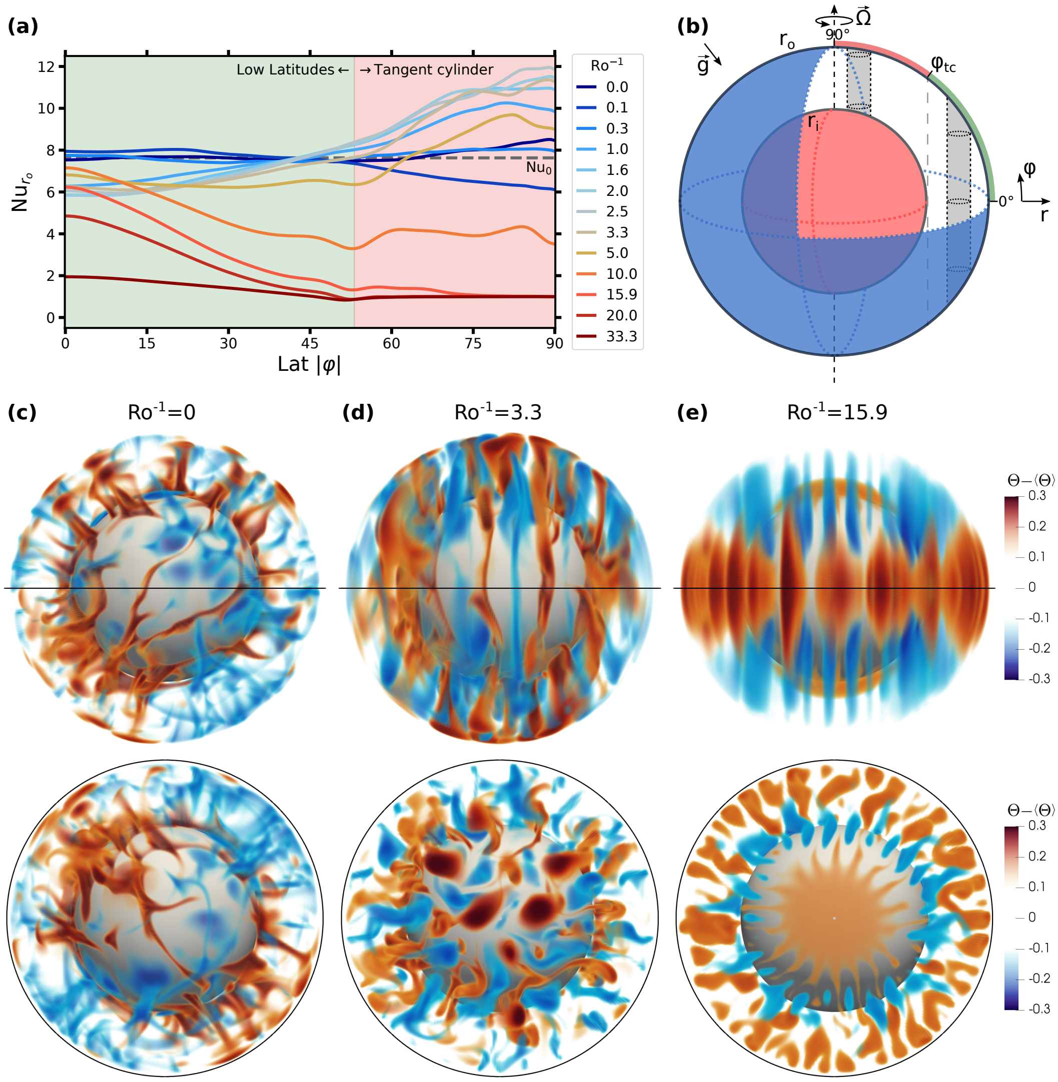

Figure 2. **(a)** Dimensionless heat transport at the outer sphere Nu_{r_o} as function of the latitude $|\varphi|$ for various rotation rates Ro^{-1} at $Ra = 10^6$ and $Pr = 4.38$ with $\eta = 0.6$ and constant $g(r) = g_0$. **(b)** Schematic view on spherical RRBC showing the idealized arrangement of axially aligned Taylor columns inside and outside the polar tangent cylinder. **(c-e)** Corresponding 3D snapshots of the temperature fluctuations $\Theta' = \Theta - \langle\Theta\rangle_{\vartheta,\varphi}$ at no rotation ($Ro^{-1} = 0$), intermediate rotation ($Ro^{-1} = 3.\bar{3}$), and rapid rotation ($Ro^{-1} = 15.9$), respectively, viewed from the equator (top) and the South pole (bottom).

becomes strongly focused in the orthogonal planes (Proudman, 1916; Taylor, 1917, 1923). Thus, convection halts inside the tangent cylinder and the radial heat transport mostly aligned with the rotation axis becomes purely conductive. Towards the equator, quasi-2D vortical motion aligns with radial buoyancy, which helps to longer sustain convective heat transport via sheet-like plumes (Fig. 2(e)). Also for rapid rotation, $|\varphi_{\mathrm{tc}}|$ depicts a major transition in the trend of $Nu_{r_o}(|\varphi|)$, namely where the heat transport starts to increase towards its equatorial peak value (Fig. 2(a), see also Wang et al., 2021; Gastine & Aurnou, 2023).

Overall, Fig. 2 shows that heat transport enhancement, as known from planar RRBC, is limited to high latitudes inside the tangent cylinder in spherical RRBC. In order to further quantify the polar enhancement, we consider the radial heat transport at the outer sphere averaged (i) over the polar region $Nu_{\mathrm{tc}} = \langle Nu_{r_o} \rangle_{|\varphi|>|\varphi_{\mathrm{tc}}|}$, (ii) in the complementary low latitude region $Nu_{\mathrm{ll}} = \langle Nu_{r_o} \rangle_{|\varphi|<|\varphi_{\mathrm{tc}}|}$, and (iii) globally over the entire sphere $\langle Nu_{r_o} \rangle_{\varphi}$. In this way, we can demonstrate that the heat transport in the polar region Nu_{tc} shows the typical enhancement behavior of planar RRBC (Fig. 3(a), red triangles). Together with the results above (Fig. 2), it becomes clear that the basic mechanisms, which cause the polar enhancement, remain the same, namely: the formation of axially coherent vortical structures bridging the bulk between the hot and the cold source, such that Ekman pumping of relatively hot/cold fluid from the boundary layers can support the heat transport along the axial direction. However, no enhancement is found for the global heat transport of the full Rayleigh-Bénard sphere (Fig. 3(a), gray circles). The enhanced heat transport inside the polar region is globally balanced by the reduced heat transport in the low latitude region (Fig. 3(a), green squares). It seems that the equatorial reduction strengthens as the polar enhancement increases.

The amplitude of polar heat transport enhancement compared to Nu_0 reaches $\approx 28\%$ (Fig. 3(a), red triangles), which is comparable with the enhancement observed in planar RRBC (e.g., Zhong et al., 2009; Kunnen et al., 2011; Yang et al., 2020). The polar enhancement is even larger when only a narrower region directly around the poles is considered (see Supporting Information Fig. S1), which emphasizes the additional influence of the tilt between buoyancy and rotation. Despite the absence of a global heat transport enhancement (relative to Nu_0 of the non-rotating system), the spatial large-scale variations of the heat transport are more important in geo- and astrophysical contexts, like the ocean dynamics of the icy moons. A direct comparison of $Nu_{\mathrm{tc}}/Nu_{\mathrm{ll}}$ yields up to $\approx 50\%$ larger heat transport in the polar region than in the low latitude region at the maximal polar enhancement (Fig. 3(b), full circles). For strong rotation this ratio inverts as convection halts earlier in the tangent cylinder and will again saturate at 1 once the system is fully in rest (Gastine & Aurnou, 2023).

4 Dependence on the Prandtl number

Heat transport enhancement relative to Nu_0 in planar RRBC essentially depends on Pr. No clear enhancement due to rotation is observed for $Pr < 1$ as the thermal boundary layer is always thinner than the kinetic Ekman layer (Stevens et al., 2010; Yang et al., 2020). To validate this Pr dependence, we conducted additional series of DNSs for $Pr = 1$ and 0.7 (see Supporting Information Tab. S3). As expected, the heat transport enhancement Nu/Nu_0 inside the polar tangent cylinder of spherical RRBC vanishes (see Supporting Information Fig. S2(a)). Interestingly, the heat transport in the low-latitude region also decreases with smaller Pr. Therefore, we can still observe some latitudinal enhancement $Nu_{\mathrm{tc}}/Nu_{\mathrm{ll}} > 1$ for $Pr = 0.7$ (see Supporting Information Fig. S2(b)) without any polar enhancement $Nu/Nu_0 < 1$. This agrees with the results from Soderlund (2019) performed at $Pr = 1$. However, the latitudinal enhancement $Nu_{\mathrm{tc}}/Nu_{\mathrm{ll}}$ is significantly smaller than for $Pr = 4.38$. Based on this trend, we conclude that, the polar enhancement Nu/Nu_0, which typically intensifies with increasing Pr above unity, will additionally amplify the latitudinal enhancement $Nu_{\mathrm{tc}}/Nu_{\mathrm{ll}}$. Since Pr also affects the heat transport in the low latitude region,

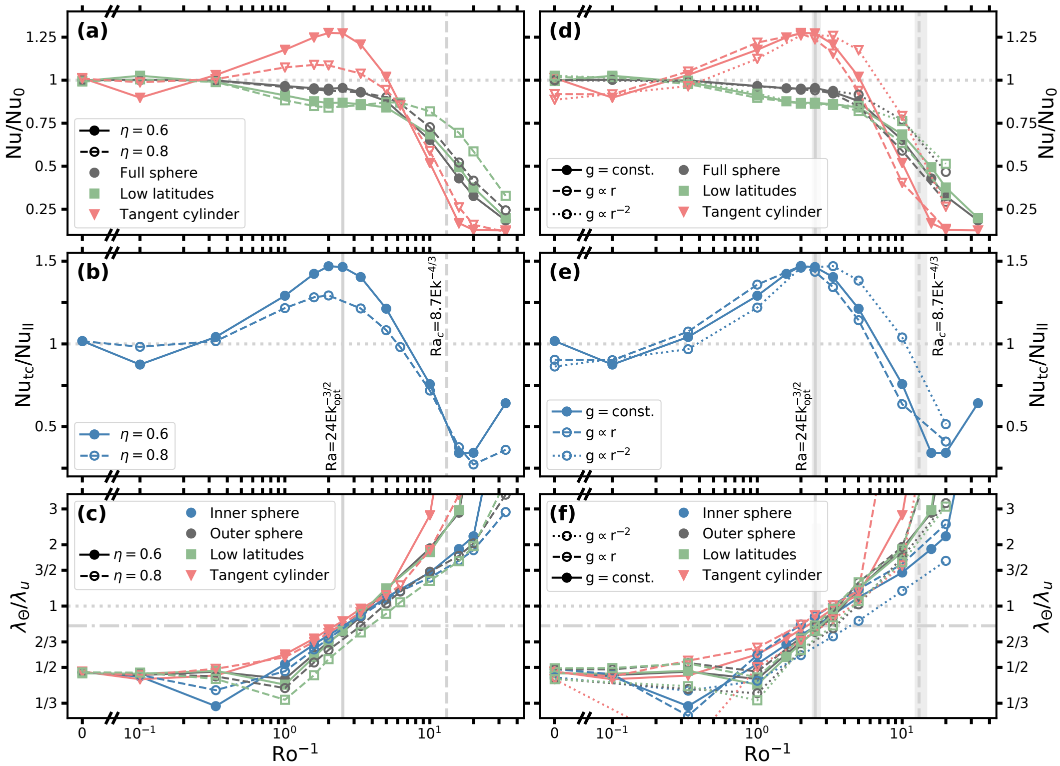

Figure 3. **(a,d)** Heat transport Nu relative to the non-rotating reference Nu_0 as a function of Ro^{-1} for the full sphere ($Nu \equiv \langle Nu_{r_o} \rangle_\varphi$), in the polar region ($Nu_{\mathrm{tc}} = \langle Nu_{r_o} \rangle_{|\varphi|>|\varphi_{\mathrm{tc}}|}$), and in the complementary low latitude region ($Nu_{\mathrm{ll}} = \langle Nu_{r_o} \rangle_{|\varphi|<|\varphi_{\mathrm{tc}}|}$). **(b,e)** Ratio between the heat transport in the polar region Nu_{tc} and the low latitude region Nu_{ll} as a function of Ro^{-1}. **(c,f)** Ratio of thermal and kinetic boundary layer thicknesses λ_Θ/λ_u as a function of Ro^{-1} averaged over the inner sphere, the outer sphere, the polar region, and the low latitude region. **(left)** For different η with constant $g(r) = g_0$, and **(right)** for different $g(r) \propto r^\gamma$ with fixed $\eta = 0.6$. All data at $Pr = 4.38$, $Ra = 10^6$. The solid and dashed vertical lines mark the predicted optimal rotation rate Ro^{-1}_{opt} in planar RRBC given by $Ra = 24Ek^{-3/2}$ (Yang et al., 2020; King et al., 2012) and the predicted onset of convection in planar RRBC given by $Ra_c = 8.7Ek^{-4/3}$ (Chandrasekhar, 1961), respectively. The influence of Ra_{eff} on these transitions (shaded areas) are very limited (see Sec. 6, 7). The dotted and dashed-dotted horizontal lines emphasize ratio 1 and 0.8, respectively.

we speculate that for $Pr \gg 1$, even an enhancement of the global heat transport Nu/Nu_0 is possible.

5 Influence of shell thickness

In fact, the oceans of icy satellites are much thinner water layers, i.e., characterized by a much larger radius ratio than the previous $\eta = 0.6$. For the popular icy satellites indicated in Fig. 1, the estimates are in a range of $0.74 < \eta < 0.99$ (Vance et al., 2018; Soderlund, 2019). A larger η also results in a larger polar tangent cylinder, in which the axial columns connect inner and outer sphere. When we increase the radius ratio to $\eta = 0.8$, the tangent cylinder starts already at $\varphi_{\mathrm{tc}} \approx 36.87$ (compared to $\varphi_{\mathrm{tc}} \approx 53.13$ for $\eta = 0.6$). Interestingly, the heat transport enhancement in the polar tangent cylinder drops to only $\approx 9\%$, whereas the full sphere average remains unchanged throughout the rotation-affected regime (Fig. 3(a), open symbols). This seems very counterintuitive since one would rather expect that a constant enhancement amplitude in the enlarged tangent cylinder, which also affects the global heat transport. We speculate that increasing inclination between radial buoyancy and axial rotation towards the edge of the tangent cylinder reduces the efficiency of vortices pumping heat in the axial direction. However, we note that even at the poles the heat transport enhancement is smaller for $\eta = 0.8$ than for $\eta = 0.6$. (see Supporting Information Fig. S3). Regardless, the heat transport in the polar region can still be significantly larger than at the equator for $\eta = 0.8$, resulting in a latitudinal enhancement up to $\approx 25\%$ (Fig. 3(b), open symbols). The optimal rotation rate Ro_{opt}^{-1} at which the maximal enhancements are achieved, however, remains mostly unaffected.

In the rotation-dominated regime, the heat transport in the polar region decreases similarly with Ro^{-1} for both η. Convection in the tangent cylinder ceases around $Ro_c^{-1} = 8.7^{-3/4} Pr^{1/2} Ra^{1/4} \approx 13.06$ (Fig. 3(a), vertical dashed line), derived from the predicted critical Rayleigh number $Ra_c = 8.7 Ek^{-4/3}$ in planar RRBC (Chandrasekhar, 1961). On the contrary, faster rotation is necessary to suppress convective heat transport in the low latitude region for larger η. Consequently, the equatorial onset of convection in spherical RRBC additionally depends on η, in contrast to Ra_c in planar RRBC valid in the likewise oriented tangent cylinder. Together with the data from Gastine et al. (2016) and Gastine and Aurnou (2023), this reflects that the equatorial onset of convection in spherical RRBC is different than in planar RRBC, i.e., $Ra_{c,sp} = f(\eta, ...)\, Ek^{-4/3}$ rather than $Ra_c = 8.7\, Ek^{-4/3}$.

Lastly, we note the different slopes of the heat transport in the polar and the low latitude region in the rotation-dominated regime. They can be attributed to “steep scaling” $Nu \propto (Ra\, Ek^{4/3})^3 \propto Ro^4$ in the polar region where Ekman puming plays an active role (King et al., 2012, 2013; Julien et al., 2016; Plumley et al., 2016; Gastine & Aurnou, 2023) and (the onset of) “diffusion-free scaling” $Nu \propto (Ra\, Ek^{4/3})^{3/2} \propto Ro^2$ (Gastine et al., 2016; Wang et al., 2021). More detailed evidence for this can be found in the Supporting Information (Text S2, Fig. S4).

6 Sensitivity to different gravity profiles

We further investigate the influence of different radial gravity profiles $g(r) = g_0\ (r/r_o)^{\gamma}$. Besides a constant gravity ($\gamma = 0$), we apply a homogeneous self-gravitating profile ($\gamma = 1$) and a mass-centered profile ($\gamma = -2$). For this, we stick to $\eta = 0.6$, because the radial gravity variation is larger in thicker shells and so is its expected impact on the heat transport. Aside from minor deviations, we cannot observe major differences in the normalized heat transport Nu/Nu_0 in the rotation-affected regime (until the polar heat transport maximum), including the amplitude of the polar and latitudinal enhancement maxima and their optimal rotation rate Ro_{opt}^{-1} (Fig. 3(d,e)). One might spot a small shift in Ro^{-1} with γ. Its trend likely arises from a change of the effective Rayleigh number of the system $Ra_{\mathrm{eff}} = \langle Ra(r) \rangle_r$, when the gravity varies with r: $Ra_{\mathrm{eff}}(\gamma = 1) < Ra_{\mathrm{eff}}(\gamma = 0) = Ra < Ra_{\mathrm{eff}}(\gamma = -2)$ (see Supporting Information Text S3). Solely in the rotation-dominant regime (beyond the polar heat transport maximum), the heat transport remains considerably larger for smaller γ, i.e., increasing Ra_{eff}. Thus, the relative heat transport enhancement Nu/Nu_0 for $Ro^{-1} \leq Ro^{-1}_{\text{opt}}$ is mostly unaffected by the gravity profile $g(r) = r^{\gamma}$, in contrast to the absolute values Nu (Gastine et al., 2015; Wang et al., 2022). Especially the amplitude of the polar enhancement maximum $Nu_{\max}/Nu_0$ seems to be insensitive to $g(r)$.

7 Relevance of the boundary layer ratio

In planar RRBC, the heat transport maximum for not too large Ra is typically associated with an equal thickness of the thermal and kinetic boundary layers λ_Θ and λ_u (Stevens et al., 2010), which theoretically scales as $\lambda_\Theta/\lambda_u \propto Ek^{3/2}Ra$ (King et al., 2012) giving an estimate for the optimal rotation rate at relatively low Ra (Yang et al., 2020):

$$Ro^{-1}_{\text{opt}} \approx 0.12\, Pr^{1/2} Ra^{1/6} \quad \text{or} \quad Ra \approx 24\, Ek^{-3/2}_{\text{opt}} \quad . \tag{6}$$

The predicted Ro^{-1}_{opt} nicely aligns with the heat transport maxima in the polar tangent cylinder independent of η and $g(r)$ (Fig. 3(a,d), solid vertical line). Taking Ra_{eff} into account yields $Ro^{-1}_{\text{opt},\gamma=1} \approx 0.97\, Ro^{-1}_{\text{opt},\gamma=0}$ and $Ro^{-1}_{\text{opt},\gamma=-2} \approx 1.07\, Ro^{-1}_{\text{opt},\gamma=0}$ (see Supporting Information Text S3). Both predicted and observed shifts of Ro^{-1}_{opt} with γ are mostly negligible.

We further verify the predicted boundary layer crossing by directly computing λ_Θ and λ_u from our DNSs as the height of the first peak in the radial profiles of the laterally averaged root-mean-square temperature and lateral velocity, respectively. Due to the asymmetry of cooling and heating in spherical RRBC, the boundary layer thicknesses differ between inner and outer sphere (Gastine et al., 2015). Therefore, we consider λ_Θ and λ_u separately averaged over (i) the inner and (ii) the outer spheres. In addition to the spatial average over the full spheres, we again distinguish between (iii) the polar and (iv) the low latitude regions on the outer sphere. Our data confirms such a typical boundary layer crossing for all the regions (i)-(iv) in the spherical geometry – independent of η (Fig. 3(c)). Furthermore, the polar heat transport maxima and the predicted Ro^{-1}_{opt} perfectly match to an observed boundary layer ratio of $\lambda_\Theta/\lambda_u \approx 0.8$ (dotted horizontal line), especially for the polar region (red symbols) and the inner sphere (blue symbols). This fully agrees with the observations of Yang et al. (2020) in planar RRBC based on the same boundary layer definitions. Only for the thinner $\eta = 0.8$ shell, the boundary layer ratio of the low latitude region (and consequently also for the full outer sphere) lie slightly below the expected $\lambda_\Theta/\lambda_u \approx 0.8$. We also relate this to the different flow orientation at the equator, where the inner and outer shells act more like a sidewall for the axial vortex structures compared to the classical configuration in planar RRBC and the alike tangent cylinder. It therefore is even more remarkable that the boundary layer ratio also matches for the low latitude region in the other cases. For variations of $g(r)$, the agreement with 0.8 is still very good (Fig. 3(f)).

8 Conclusions

Our DNSs of spherical RRBC with Pr larger than unity ($Pr = 4.38$) confirm the main features of heat transport enhancement, as known from planar RRBC, to similarly occur in the spherical geometry:

(i) The three major regimes (buoyancy-dominated, rotation-affected, rotation-dominated) for the heat transport behavior of RRBC can be identified (Kunnen, 2021; Ecke & Shishkina, 2023).

(ii) *Intermediate* rotation enhances the heat transport up to $\approx 28\%$ compared to the non-rotating case inside the polar tangent cylinder, where buoyancy is mostly aligned with the rotation axis and axially coherent vortices (Taylor columns) connect the hot inner with the cold outer shell.

(iii) The maximal (polar) enhancement is determined by an equal thickness of the thermal and kinetic boundary layers $\lambda_\Theta/\lambda_u \approx 1$. The associated optimal rotation rate $Ro_{\rm opt}^{-1} \Leftrightarrow Ek_{\rm opt}^{-1}$ can still be predicted via $Ra \approx 24\,Ek^{-3/2}$ as in planar RRBC (King et al., 2012; Yang et al., 2020).

We however find that the polar heat transport enhancement is accompanied by a reduced heat transport at low latitudes outside the tangent cylinder, where buoyancy is mostly orthogonal to the rotation axis and the axially coherent vortices can only connect both hemispheres of the cold outer shell. The equatorial reduction compensates the polar enhancement on the global average on the one hand, which on the other hand results in an even larger latitudinal enhancement of up to $\approx 50\%$ between the polar and the low latitude region.

We further clarified that the relative heat transport enhancements Nu/Nu_0 and $Nu_{\rm tc}/Nu_{\rm ll}$ are mostly unaffected by the radial gravity profile. Rather surprisingly, a thinner shell ($\eta = 0.8$), which comes along with a larger tangent cylinder, shows less but still significant enhancement ($\approx 9\%$ for Nu/Nu_0 and $\approx 25\%$ for $Nu_{\rm tc}/Nu_{\rm ll}$). The fact that the polar enhancement decreases to remain balanced by the equatorial reduction depicts a non-trivial coupling between the polar and the low latitude region in spherical RRBC.

The existence of polar heat transport enhancement in spherical RRBC, which increases the latitudinal difference between polar and equatorial heat transport, implies that accounting for $Pr > 1$ can be crucial for simulations of icy satellite oceans. Heat transport enhancement on the one hand increases with larger Pr (e.g., Zhong et al., 2009; Stevens et al., 2010) but on the other hand decreases with larger Ra (e.g., Yang et al., 2020). Hence, the question on how much enhancement persists on icy satellites with $Pr > 4.38$ ($10 \lesssim Pr \lesssim 13$) and $Ra \gg 10^6$ ($10^{16} \lesssim Ra \lesssim 10^{24}$) needs to be addressed differently as DNS cannot reach these parameters. However, our findings show, in line with evidences from previous studies (Soderlund, 2019; Amit et al., 2020; Bire et al., 2022), that in principle large Pr related heat transport enhancement could serve as an explanation for latitudinal heat transport and associated ice thickness variations on icy satellites.

Open Research Section

Data availability statement

The data that support the findings of this study are openly available in *4TU.ResearchData* at `http://doi.org/tba_on_publication`.

Acknowledgments

This work was funded by the ERC Starting Grant *UltimateRB* No. 804283. We acknowledge the access to several computational resources, all of which were used for this work: PRACE for awarding us access to MareNostrum4 at the Barcelona Supercomputing Center (BSC), Spain and IRENE at Très Grand Centre de Calcul (TGCC) du CEA, France (project 2021250115), and EuroHPC for awarding us access to Discoverer at Sofiatech, Bulgaria (No. EHPC-REG-2022R03-208).

References

Aguirre Guzmán, A. J., Madonia, M., Cheng, J. S., Ostilla-Mónico, R., Clercx, H. J., & Kunnen, R. P. (2020). Competition between Ekman Plumes and Vortex Condensates in Rapidly Rotating Thermal Convection. *Phys. Rev. Lett.*, *125*, 214501.

Ahlers, G., Grossmann, S., & Lohse, D. (2009). Heat transfer and large scale dynamics in turbulent Rayleigh-Bénard convection. *Rev. Mod. Phys.*, *81*, 503–537.

Amit, H., Choblet, G., Tobie, G., Terra-Nova, F., Čadek, O., & Bouffard, M. (2020). Cooling

patterns in rotating thin spherical shells — Application to Titan's subsurface ocean. *ICARUS*, *338*, 113509.
Aurnou, J., Calkins, M., Cheng, J., Julien, K., King, E., Nieves, D., ... Stellmach, S. (2015). Rotating convective turbulence in Earth and planetary cores. *Phys. Earth Planet. Inter.*, *246*, 52–71.
Beuthe, M., Rivoldini, A., & Trinh, A. (2016). Enceladus's and Dione's floating ice shells supported by minimum stress isostasy. *Geophys. Res. Lett.*, *43*(19), 10,088–10,096.
Bire, S., Kang, W., Ramadhan, A., Campin, J., & Marshall, J. (2022). Exploring Ocean Circulation on Icy Moons Heated From Below. *J. Geophys. Res. Planets*, *127*(3).
Busse, F. H. (1970). Thermal instabilities in rapidly rotating systems. *J. Fluid Mech.*, *44*(3), 441–460.
Busse, F. H. (1983). A model of mean zonal flows in the major planets. *Geophys. Astrophys. Fluid Dyn.*, *23*(2), 153–174.
Chandrasekhar, S. (1961). *Hydrodynamic and hydromagnetic stability.* Oxford University Press.
Cheng, J. S., Stellmach, S., Ribeiro, A., Grannan, A., King, E. M., & Aurnou, J. M. (2015). Laboratory-numerical models of rapidly rotating convection in planetary cores. *Geophys. J. Int.*, *201*, 1–17.
Chyba, C. F., & Hand, K. P. (2005). Astrobiology: The Study of the Living Universe. *Annu. Rev. Astron. Astrophys.*, *43*(1), 31–74.
Ecke, R. E., & Niemela, J. J. (2014). Heat Transport in the Geostrophic Regime of Rotating Rayleigh-Bénard Convection. *Phys. Rev. Lett.*, *113*, 114301.
Ecke, R. E., & Shishkina, O. (2023). Turbulent Rotating Rayleigh-Bénard Convection. *Annu. Rev. Fluid Mech.*, *55*, 603-38.
Gastine, T., & Aurnou, J. M. (2023). Latitudinal regionalization of rotating spherical shell convection. *J. Fluid Mech.*, *954*, R1.
Gastine, T., Wicht, J., & Aubert, J. (2016). Scaling regimes in spherical shell rotating convection. *J. Fluid Mech.*, *808*, 690–732.
Gastine, T., Wicht, J., & Aurnou, J. M. (2015). Turbulent Rayleigh–Bénard convection in spherical shells. *J. Fluid Mech.*, *778*, 721–764.
Hemingway, D. J., & Mittal, T. (2019). Enceladus's ice shell structure as a window on internal heat production. *ICARUS*, *332*, 111–131.
Julien, K., Aurnou, J. M., Calkins, M. A., Knobloch, E., Marti, P., Stellmach, S., & Vasil, G. M. (2016). A nonlinear model for rotationally constrained convection with Ekman pumping. *J. Fluid Mech.*, *798*, 50–87.
Julien, K., Knobloch, E., Rubio, A. M., & Vasil, G. M. (2012). Heat transport in low-Rossby-number Rayleigh-Bénard convection. *Phys. Rev. Lett.*, *109*(25), 254503.
Julien, K., Legg, S., McWilliams, J., & Werne, J. (1996). Rapidly rotating Rayleigh-Bénard convection. *J. Fluid Mech.*, *322*, 243–273.
Julien, K., Rubio, A., Grooms, I., & Knobloch, E. (2012). Statistical and physical balances in low Rossby number Rayleigh-Bénard convection. *Geophys. Astrophys. Fluid Dyn.*, *106*, 392–428.
Kang, W. (2022). Different Ice-shell Geometries on Europa and Enceladus due to Their Different Sizes: Impacts of Ocean Heat Transport. *Astrophys. J.*, *934*(2), 116.
Kang, W., & Jansen, M. (2022). On Icy Ocean Worlds, Size Controls Ice Shell Geometry. *Astrophys. J.*, *935*(2), 103.
Kihoulou, M., Čadek, O., Kvorka, J., Kalousová, K., Choblet, G., & Tobie, G. (2023). Topographic response to ocean heat flux anomaly on the icy moons of Jupiter and Saturn. *ICARUS*, *391*, 115337.
King, E. M., Stellmach, S., & Aurnou, J. M. (2012). Heat transfer by rapidly rotating Rayleigh-Bénard convection. *J. Fluid Mech.*, *691*, 568–582.
King, E. M., Stellmach, S., & Buffett, B. (2013). Scaling behaviour in Rayleigh-Bénard convection with and without rotation. *J. Fluid Mech.*, *717*, 449–471.
Kunnen, R. P. J. (2021). The geostrophic regime of rapidly rotating turbulent convection. *J. Turbul.*, *22*, 267-296.

Kunnen, R. P. J., Clercx, H. J. H., & Geurts, B. J. (2006). Heat flux intensification by vortical flow localization in rotating convection. *Phys. Rev. E*, *74*, 056306.
Kunnen, R. P. J., Stevens, R. J. A. M., Overkamp, J., Sun, C., Heijst, G. J. F. v., & Clercx, H. J. H. (2011). The role of Stewartson and Ekman layers in turbulent rotating Rayleigh-Bénard convection. *J. Fluid Mech.*, *688*, 422–442.
Nimmo, F., & Pappalardo, R. T. (2016). Ocean worlds in the outer solar system. *J. Geophys. Res. Planets*, *121*(8), 1378–1399.
Plumley, M., & Julien, K. (2019). Scaling Laws in Rayleigh-Bénard Convection. *Earth Space Sci.*, *6*(9), 1580–1592.
Plumley, M., Julien, K., Marti, P., & Stellmach, S. (2016). The effects of Ekman pumping on quasi-geostrophic Rayleigh-Bénard convection. *J. Fluid Mech.*, *803*, 51–71.
Proudman, J. (1916). On the motion of solids in a liquid possessing vorticity. *Proc. R. Soc. London A*, *92*, 408–424.
Roberts, P. H. (1968). On the thermal instability of a rotating-fluid sphere containing heat sources. *Philos. Trans. R. Soc. A*, *263*(1136), 93–117.
Rossby, H. T. (1969). A study of Bénard convection with and without rotation. *J. Fluid Mech.*, *36*, 309–335.
Santelli, L., Orlandi, P., & Verzicco, R. (2020). A finite-difference scheme for three-dimensional incompressible flows in spherical coordinates. *J. Comput. Phys.*, *424*, 109848.
Shishkina, O., Stevens, R. J. A. M., Grossmann, S., & Lohse, D. (2010). Boundary layer structure in turbulent thermal convection and its consequences for the required numerical resolution. *New J. Phys.*, *12*, 075022.
Soderlund, K. M. (2019). Ocean Dynamics of Outer Solar System Satellites. *Geophys. Res. Lett.*, *46*, 8700–8710.
Soderlund, K. M., King, E. M., & Aurnou, J. M. (2012). The influence of magnetic fields in planetary dynamo models. *Earth Planet. Sci. Lett.*, *333-334*, 9–20.
Sprague, M., Julien, K., Knobloch, E., & Werne, J. (2006). Numerical simulation of an asymptotically reduced system for rotationally constrained convection. *J. Fluid Mech.*, *551*, 141–174.
Stellmach, S., Lischper, M., Julien, K., Vasil, G., Cheng, J. S., Ribeiro, A., … Aurnou, J. M. (2014). Approaching the Asymptotic Regime of Rapidly Rotating Convection: Boundary Layers versus Interior Dynamics. *Phys. Rev. Lett.*, *113*, 254501.
Stevens, R. J. A. M., Blass, A., Zhu, X., Verzicco, R., & Lohse, D. (2018). Turbulent thermal superstructures in Rayleigh-Bénard convection. *Phys. Rev. Fluids*, *3*, 041501(R).
Stevens, R. J. A. M., Clercx, H. J. H., & Lohse, D. (2010). Optimal Prandtl number for heat transfer in rotating Rayleigh-Bénard convection. *New J. Phys.*, *12*, 075005.
Stevens, R. J. A. M., Clercx, H. J. H., & Lohse, D. (2013). Heat transport and flow structure in rotating Rayleigh-Bénard convection. *Eur. J. Mech. B/Fluids*, *40*, 41–49.
Stevens, R. J. A. M., Zhong, J.-Q., Clercx, H. J. H., Ahlers, G., & Lohse, D. (2009). Transitions between turbulent states in rotating Rayleigh-Bénard convection. *Phys. Rev. Lett.*, *103*, 024503.
Taylor, G. I. (1917). Motion of solids in fluids when the flow is not irrotational. *Proc. R. Soc. London A*, *93*(648), 99-113.
Taylor, G. I. (1923). Stability of a viscous liquid contained between two rotating cylinders. *Phil. Trans. R. Soc. A*, *223*, 289–343.
Vance, S. D., Panning, M. P., Stähler, S., Cammarano, F., Bills, B. G., Tobie, G., … Banerdt, B. (2018). Geophysical Investigations of Habitability in Ice-Covered Ocean Worlds. *J. Geophys. Res. Planets*, *123*(1), 180–205.
van der Poel, E. P., Stevens, R. J. A. M., & Lohse, D. (2013). Comparison between two and three dimensional Rayleigh-Bénard convection. *J. Fluid Mech.*, *736*, 177–194.
Wang, G., Santelli, L., Lohse, D., Verzicco, R., & Stevens, R. J. A. M. (2021). Diffusion-free scaling in rotating spherical Rayleigh-Bénard convection. *Geophys. Res. Lett.*, *48*(20), e2021GL095017.

Wang, G., Santelli, L., Verzicco, R., Lohse, D., & Stevens, R. J. A. M. (2022). Off-centre gravity induces large-scale flow patterns in spherical Rayleigh–Bénard convection. *J. Fluid Mech.*, *942*, A21.

Weiss, S., Stevens, R. J. A. M., Zhong, J.-Q., Clercx, H. J. H., Lohse, D., & Ahlers, G. (2010). Finite-size effects lead to supercritical bifurcations in turbulent rotating Rayleigh-Bénard convection. *Phys. Rev. Lett.*, *105*, 224501.

Weiss, S., Wei, P., & Ahlers, G. (2016). Heat-transport enhancement in rotating turbulent Rayleigh-Bénard convection. *Phys. Rev. E*, *93*, 043102.

Yang, Y., Verzicco, R., Lohse, D., & Stevens, R. J. A. M. (2020). What rotation rate maximizes heat transport in rotating Rayleigh-Bénard convection with Prandtl number larger than one? *Phys. Rev. Fluids*, *5*(5), 053501.

Zhong, J.-Q., Stevens, R. J. A. M., Clercx, H. J. H., Verzicco, R., Lohse, D., & Ahlers, G. (2009). Prandtl-, Rayleigh-, and Rossby-number dependence of heat transport in turbulent rotating Rayleigh-Bénard convection. *Phys. Rev. Lett.*, *102*, 044502.

Čadek, O., Souček, O., Běhounková, M., Choblet, G., Tobie, G., & Hron, J. (2019). Long-term stability of Enceladus' uneven ice shell. *ICARUS*, *319*, 476–484.

Towards understanding polar heat transport enhancement in sub-glacial oceans on icy moons

Robert Hartmann[1], **Richard J. A. M. Stevens**[1], **Detlef Lohse**[1,2], **and Roberto Verzicco**[1,3,4]

[1]Physics of Fluids Group and Twente Max Planck Center, J.M. Burgers Center for Fluid Dynamics, University of Twente, 7500 AE Enschede, The Netherlands
[2]Max Planck Institute for Dynamics and Self-Organisation, 37077 Göttingen, Germany
[3]Dipartimento di Ingegneria Industriale, University of Rome 'Tor Vergata', 00133 Rome, Italy
[4]Gran Sasso Science Institute, 67100 L'Aquila, Italy

Key Points:

- The polar heat transport in spherical rotating Rayleigh-Bénard convection experiences an enhancement by rotation.
- The influence of rotation differs at low latitudes: the heat flux is reduced and compensates the polar enhancement on the global average.
- Enhanced polar heat transport due to Ekman pumping through axial vortices could explain various phenomena on icy moons.

Corresponding author: Robert Hartmann, `r.hartmann@utwente.nl`

Abstract

The interior oceans of several icy moons are considered as "moderately rotating". Observations suggest a larger heat transport around the poles than at the equator. Rotating Rayleigh-Bénard convection (RRBC) in planar configuration is known to show an enhanced heat transport compared to the non-rotating case for such "moderate" rotation. We investigate the potential for such a (polar) heat transport enhancement in these sub-glacial oceans by direct numerical simulations of RRBC in spherical geometry for $Ra = 10^6$ and $0.7 \leq Pr \leq 4.38$. We find an enhancement up to 28% in the "polar tangent cylinder", which is globally compensated by a reduced heat transport at low latitudes. As a result, the polar heat transport can exceed the equatorial by up to 50%. The enhancement is mostly insensitive to different radial gravity profiles, but decreases for thinner shells. In general, polar heat transport and its enhancement in spherical RRBC follow the same principles as in planar RRBC.

Plain Language Summary

The icy moons of Jupiter and Saturn like e.g., Europa, Titan, or Enceladus are believed to have a water ocean beneath their ice crust. Several of them show phenomena in their polar regions like active geysers or a thinner crust than at the equator, all of which might be related to a larger heat transport around the poles from the underlying ocean. We simulate the flow dynamics and currents in these sub-glacial ocean by high-fidelity simulations, though still at less extreme parameters than in reality, to study the heat transport and provide a possible explanation of such a "polar heat transport enhancement". We find that the heat transport around the poles can be up to 50% larger than around the equator, and that the believed properties of the icy moons and their oceans would allow polar heat transport enhancement. Therefore, our results may help to improve the understanding of ocean currents and latitudinal variations in the oceanic heat transport and crustal thickness on icy moons.

1 Introduction

In the common understanding, most icy satellites in the solar system, e.g., the Jovian and Saturnian moons Europa, Ganymede, Titan, and Enceladus, contain a global ocean layer beneath their ice crust (e.g., Nimmo & Pappalardo, 2016), which gained a lot of interest in terms of habitable environments (e.g., Chyba & Hand, 2005; Vance et al., 2018). In order to asses their habitability, it is crucial to understand their flow dynamics. On Enceladus, for instance, eruptions from fault systems at the south pole (see, e.g., Nimmo & Pappalardo, 2016) suggest a strong polar anomaly of enhanced heat transport. Furthermore, the crustal thickness counterintuitively decreases from the equator towards the poles (e.g., Beuthe et al., 2016; Čadek et al., 2019; Hemingway & Mittal, 2019; Kang, 2022; Kang & Jansen, 2022), which suggests a large-scale latitudinal variation of the heat released from the sub-glacial ocean (Kihoulou et al., 2023). In this study, we investigate the dynamics inside and the heat transport out of these oceans by direct numerical simulations (DNSs) of rotating Rayleigh-Bénard convection (RRBC) in spherical geometry. Therewith, we aim to provide a possible explanation for the origin of the polar enhancement of the heat transport on icy moons.

The canonical system of RRBC in planar configuration has been extensively studied experimentally and numerically (see, e.g., the reviews by Kunnen, 2021; Ecke & Shishkina, 2023; Stevens et al., 2013; Plumley & Julien, 2019, and Refs. therein). Its dynamical behavior is fully controlled by three dimensionless parameters: the Prandtl number Pr describing the fluid properties, the Rayleigh number Ra setting the strength of thermal driving, and the inverse Rossby number Ro^{-1} as a measure for the importance of rotation relative to buoyancy (full definitions in Sec. 2). The influence of rotation can alternatively be parameterized by the Ekman number $Ek = Ro\sqrt{Pr/Ra}$. Several flow regimes and

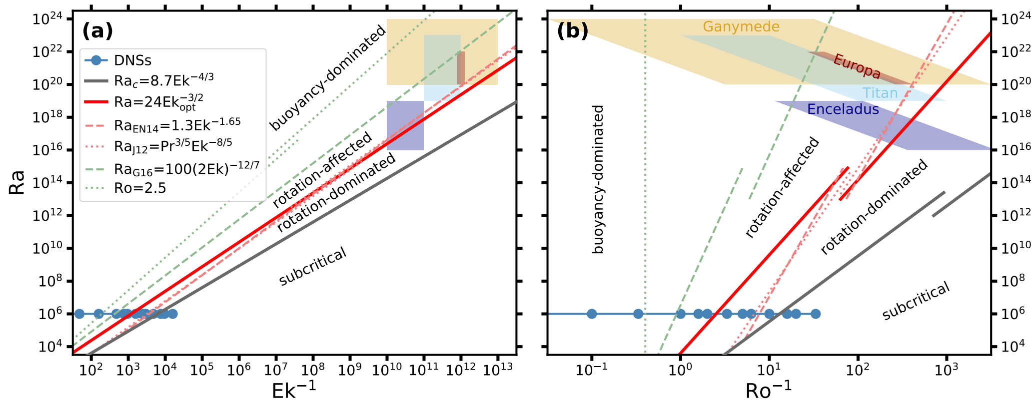

Figure 1. Regime diagram of (planar) RRBC in the parameter space of **(a)** Ra and Ek^{-1} and **(b)** Ra and Ro^{-1} (after Soderlund (2019), see also Kunnen (2021)): The solid gray line denotes the critical Rayleigh number Ra_c for the onset of convection (Chandrasekhar, 1961). The solid red line depicts the transition between the rotation-dominated and the rotation-affected regimes for based on boundary layer crossing and heat transport maximum per fixed Ra for $Pr > 1$ fluids (Yang et al., 2020). Dashed and dotted light red lines are alternative estimates for this transition by Ecke and Niemela (2014) and Julien, Knobloch, et al. (2012), respectively. The dashed and dotted green lines represent the transition between the rotation-affected and the buoyancy-dominated regimes based on Gastine et al. (2016) and for a cylinder with diameter-to-height ratio 1 (Weiss et al., 2010), respectively. The blue circles mark the simulations of spherical RRBC in this study ($Pr = 4.38$). The shaded areas show the predicted parameter range for several icy moons ($10 \leq Pr \leq 13$) as given in (Soderlund, 2019). Line offsets symbolize the Pr dependence of any transition between $Pr = 4.38$ like in our simulations and $Pr = 13$ like the upper bound for the icy moons.

flow states were discovered and studied over the past decades. The three major regimes based on the trend of heat transport with variying rotation are (i) the *buoyancy-dominated* regime at relatively slow rotation, where heat transport and flow dynamics remain unaffected compared to the non-rotating case, (ii) the transitional *rotation-affected* regime, where intermediate or moderate rotation starts to alter the flow, and (iii) the *rotation-dominated* regime for rapid rotation, where the heat transport steeply decreases with increasing rotation that impedes vertical motion (Proudman, 1916; Taylor, 1917), see e.g., Kunnen (2021) and Ecke and Shishkina (2023). Both rotation-affected and rotation-dominated regimes show a broad variety of sub-regimes or flow states, all of which are characterized by columnar vortical structures aligned with the rotation axis (e.g., Julien et al., 1996; Sprague et al., 2006; Stevens et al., 2009; Julien, Rubio, et al., 2012; Stellmach et al., 2014; Cheng et al., 2015; Aguirre Guzmán et al., 2020). Due to the huge variety of flow states, there exist various estimates for the boundaries of the above regimes in the literature (see Kunnen (2021) for a detailed overview) - most of them based on RRBC data in the classical planar configuration. The most common ones are summarized Fig. 1.

An important peculiarity of planar RRBC with $Pr > 1$ is that Ekman pumping through vertically coherent vortices enhances the heat transport in the rotation-affected regime to exceed its non-rotating value (e.g., Rossby, 1969; Kunnen et al., 2006; Zhong et al., 2009; Stevens et al., 2013). For not too large Ra, the enhancing effect is most efficient when thermal and kinetic boundary layers have approximately the same thickness (Stevens et al., 2010; Yang et al., 2020). This creates a heat transport maximum (per fixed Ra) that follows $Ra \propto Ek^{-3/2}$ (Fig. 1, red line; King et al., 2012; Yang et al., 2020). For very turbulent flows, the maximum diverges towards weaker rotation (Yang et al., 2020).

Based on the estimated parameter ranges for Europa, Ganymede, Titan, and Enceladus by Soderlund (2019), their sub-glacial oceans most likely are in the rotation-affected regime (see Fig. 1). Given that the water of these oceans has $Pr \in [10, 13]$ (Soderlund, 2019), they arguably have the potential for heat transport enhancement - at least around the poles, where buoyancy is mostly aligned with the rotation axis as it is in planar RRBC. Evidence of such a polar heat transport enhancement spherical RRBC are present in several studies (Soderlund, 2019; Amit et al., 2020; Bire et al., 2022). We therefore distinguish between two types of heat transport enhancement: (i) enhancement above the non-rotating heat transport in a specific region is considered as *polar/global/... enhancement*, whereas (ii) a larger heat transport at the poles than at the equator is referred to as *latitudinal enhancement*. Since most simulations of spherical RRBC are conducted for $Pr = 1$ (e.g., Soderlund et al., 2012; Gastine et al., 2016; Wang et al., 2021) and all studies on rotation-induced heat transport enhancement focus on planar RRBC (e.g., Stevens et al., 2009, 2010; Weiss et al., 2016; Yang et al., 2020), we aim to bridge this gap and elucidate the potential of spherical RRBC to show polar and/or global heat transport enhancement. Therefore, we set $Pr = 4.38$ as in many simulations and experiments of planar RRBC and cover the entire range of regimes (Fig. 1).

In the following, we introduce spherical RRBC, its control parameters, and our numerical method (Sec. 2). Then, latitudinal variations of the heat transport are analyzed and linked to the predominant structures in the flow (Sec. 3). Subsequently, we discuss the importance of $Pr > 1$ by a direct comparison with $Pr \leq 1$ (Sec. 4), the influence of the shell thickness, i.e., the ocean depth (Sec. 5), the sensitivity to different radial gravity profiles (Sec. 6), and the relevance of the ratio between thermal and kinetic boundary layers for heat transport enhancement in spherical RRBC (Sec. 7). The letter ends with conclusions (Sec. 8).

2 Dynamical equations and numerical method

Spherical RRBC describes the dynamics of a fluid in a spherical shell confined by a hot inner and a cold outer sphere, rotating around a polar axis (Fig. 2(b)) (e.g., Roberts, 1968; Busse, 1970, 1983; Aurnou et al., 2015). The geometry of the system is determined by the inner and outer radii r_i and r_o, defining the shell thickness $H = r_o - r_i$ expressed by the radius ratio $\eta = r_i/r_o$. The dynamics are controlled by the three dimensionless parameters Pr, Ra, and Ro^{-1}, defined as:

$$Pr = \frac{\nu}{\kappa} \ , \ Ra = \frac{\alpha g_0 \Delta T H^3}{\nu\kappa} \ , \ Ro^{-1} = \frac{2\Omega H}{\sqrt{\alpha g_0 \Delta T H}} \ . \tag{1}$$

Therein, ν is the kinematic viscosity, κ the thermal diffusivity, α the isobaric thermal expansion coefficient, g_0 the reference gravitational acceleration at the outer sphere, ΔT the temperature difference between inner and outer sphere, and Ω the angular rotation rate, respectively. Under Oberbeck-Boussinesq approximation, the system is governed by the continuity, Navier-Stokes and temperature convection-diffusion equations, which are given in dimensionless form as:

$$\nabla \cdot \vec{u} = 0 \ , \tag{2}$$

$$\frac{\mathrm{d}\vec{u}}{\mathrm{d}t} = -\nabla P + \sqrt{\frac{Pr}{Ra}} \nabla^2 \vec{u} + \Theta \frac{g(r)}{g_0} \vec{e}_r - \frac{1}{Ro} \vec{e}_z \times \vec{u} \ , \tag{3}$$

$$\frac{\mathrm{d}\Theta}{\mathrm{d}t} = \frac{1}{\sqrt{Pr\,Ra}} \nabla^2 \Theta \ . \tag{4}$$

Therein, $\vec{u}$, P, and Θ denote the normalized velocity, pressure, and temperature fields, respectively. $\mathrm{d}/\mathrm{d}t$ denotes the full, so-called material derivative. $g(r) = g_0\,(r/r_o)^\gamma$ accounts for radial variations in the gravity profile. The equations are normalized by H and the free-fall velocity $U_0 = \sqrt{\alpha g_0 \Delta T H}$. The temperature is normalized as $\Theta = \frac{T - T_{\mathrm{top}}}{\Delta T} \in [0, 1]$. The pressure field P is reduced by the hydrostatic balance and centrifugal contributions. We consider Coriolis forcing from constant rotation around the polar axis, but neglect centrifugal contributions on buoyancy. Isothermal and no-slip boundary conditions are imposed at the hot inner ($\Theta = 1$) and the cold outer ($\Theta = 0$) spheres.

In this study we conduct direct numerical simulations (DNSs) for $Ra = 10^6$ at $Pr =$ 4.38, 1 and 0.7 while varying the radius ratio η and gravity profile $g(r)$. The DNSs solve the governing equations (Eqs. 2-4) by a central second-order accurate finite-difference scheme based on a staggered grid discretization in spherical coordinates (Santelli et al., 2020), which has been rigorously validated in subsequent studies (Wang et al., 2021, 2022). The computational grid is uniformly spaced in the longitudinal and latitudinal directions, while the grid points in the radial direction are clustered towards the inner and outer spheres. This ensures an appropriate resolution of the Kolmogorov scales in the bulk, as well as of the boundary layers (Shishkina et al., 2010). A summary of grid sizes and numerical parameters can be found in the Supporting Information (Text S1, Tabs. S1-S3).

3 Polar heat transport enhancement

We begin our investigation on a rather thick shell of $\eta = 0.6$ with a constant gravity $g(r) = g_0$. The dimensionless heat transport is given by the Nusselt number Nu. We first consider Nu on the outer sphere as a function of the latitude φ:

$$Nu_{r_o}(|\varphi|) = -\frac{1}{\eta}\partial_r \left.\langle\Theta\rangle_{t,\vartheta,\pm\varphi}\right|_{r_o} . \tag{5}$$

Therein $\langle\cdot\rangle_{t,\vartheta,\pm\varphi}$ indicates averaging in time, longitude, and latitudinal symmetry around the equator. For no and slow rotation ($Ro^{-1} \leq 0.3$), the heat transport is expectably uniform over φ (Fig. 2(a)). Accordingly, the flow is dominated by radial buoyant plumes (Fig. 2(c)), which can organize in a persistent large-scale circulation pattern. Such large-scale circulations are well known from other non-rotating geometries, e.g., RBC in cylindrical containers (e.g., Ahlers et al., 2009, and Refs. therein), 2D RBC (e.g., van der Poel et al., 2013, and Refs. therein), or extremely wide domains (Stevens et al., 2018). However, without rotation, the heat transport ideally is radially symmetric, defining a reference value $Nu_0 = \langle Nu_{r_o}\rangle_\varphi (Ro^{-1} = 0)$ (Fig. 2(a), horizontal dashed line).

At intermediate rotation rates ($1 \leq Ro^{-1} \leq 5$), the heat transport is reduced towards the equator and enhanced towards the poles compared to the non-rotating reference (Fig. 2(a)). Taylor columns aligned with the rotation axis form in the flow (Fig. 2(d)) and alter the heat transport. Their vortical motion impedes the radial heat transport around the equator and leads to the formation of sheet-like thermal plumes around the columnar structures (similar to Soderlund et al., 2012; Aurnou et al., 2015). On the contrary, the Taylor columns support the radial heat transport around the poles by Ekman pumping through their interior (in presence of no-slip boundary conditions, e.g., Stellmach et al. (2014)). For $\eta = 0.6$, the polar tangent cylinder, i.e., the cylinder around the inner sphere aligned with the polar axis, intersects with the outer sphere at latitude $|\varphi_{\mathrm{tc}}| = 53.13°$. We use $|\varphi_{\mathrm{tc}}|$ to distinguish between the "polar region" ($|\varphi_{\mathrm{tc}}| < |\varphi| < 90°$), in which ideal axial Taylor columns connect the hot inner sphere with cold outer sphere, and the "low latitude region" ($|\varphi_{\mathrm{tc}}| > |\varphi| > 0°$), in which axial Taylor columns connect the Northern and Southern hemispheres of the outer sphere (Fig. 2(b)). For $1 \leq Ro^{-1} \leq 5$, $|\varphi_{\mathrm{tc}}|$ clearly correlates with the transition from reduced to enhanced heat transport ($Nu_{r_o}(|\varphi_{\mathrm{tc}}|) \approx Nu_0$). The rather smooth trend of $Nu_{r_o}(|\varphi|)$ across $|\varphi_{\mathrm{tc}}|$ however suggests that the inclination between buoyancy (radial) and rotation (axial) additionally influences the enhancement with latitude.

For rapid rotation ($Ro^{-1} \geq 10$), the latitudinal trend in the heat transport is inverted (Fig. 2(a)). At high latitudes, the heat transport quickly decreases with increasing Ro^{-1} down to $Nu_{r_o} = 1$. Towards the equator, the heat transport first increases slightly (compared to the reduction at intermediate rotation), before it also decreases with increasing Ro^{-1}. With increasing rotation the fluid motion is suppressed in the axial direction and

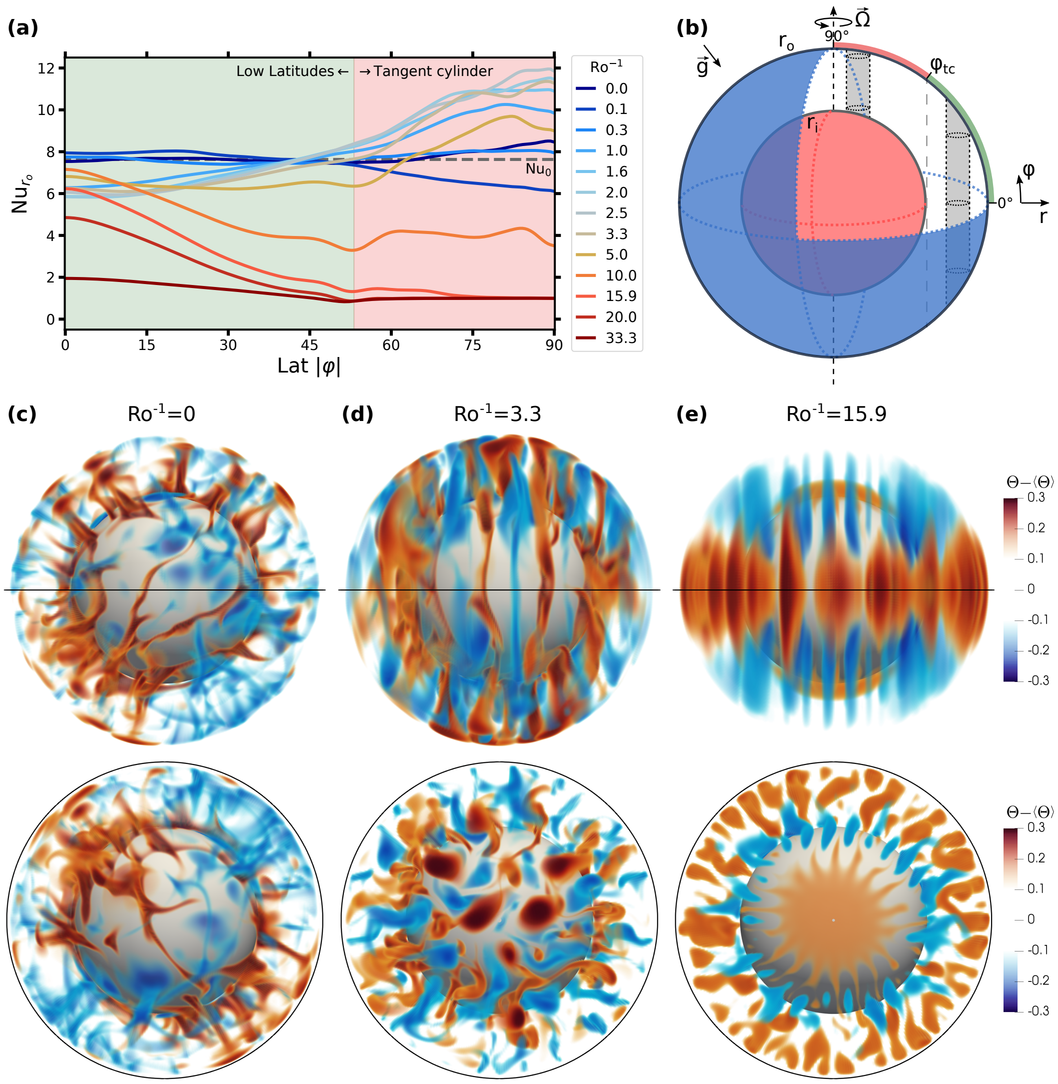

Figure 2. **(a)** Dimensionless heat transport at the outer sphere Nu_{r_o} as function of the latitude $|\varphi|$ for various rotation rates Ro^{-1} at $Ra = 10^6$ and $Pr = 4.38$ with $\eta = 0.6$ and constant $g(r) = g_0$. **(b)** Schematic view on spherical RRBC showing the idealized arrangement of axially aligned Taylor columns inside and outside the polar tangent cylinder. **(c-e)** Corresponding 3D snapshots of the temperature fluctuations $\Theta' = \Theta - \langle\Theta\rangle_{\vartheta,\varphi}$ at no rotation ($Ro^{-1} = 0$), intermediate rotation ($Ro^{-1} = 3.\bar{3}$), and rapid rotation ($Ro^{-1} = 15.9$), respectively, viewed from the equator (top) and the South pole (bottom).

becomes strongly focused in the orthogonal planes (Proudman, 1916; Taylor, 1917, 1923). Thus, convection halts inside the tangent cylinder and the radial heat transport mostly aligned with the rotation axis becomes purely conductive. Towards the equator, quasi-2D vortical motion aligns with radial buoyancy, which helps to longer sustain convective heat transport via sheet-like plumes (Fig. 2(e)). Also for rapid rotation, $|\varphi_{\rm tc}|$ depicts a major transition in the trend of $Nu_{r_o}(|\varphi|)$, namely where the heat transport starts to increase towards its equatorial peak value (Fig. 2(a), see also Wang et al., 2021; Gastine & Aurnou, 2023).

Overall, Fig. 2 shows that heat transport enhancement, as known from planar RRBC, is limited to high latitudes inside the tangent cylinder in spherical RRBC. In order to further quantify the polar enhancement, we consider the radial heat transport at the outer sphere averaged (i) over the polar region $Nu_{\rm tc} = \langle Nu_{r_o}\rangle_{|\varphi|>|\varphi_{\rm tc}|}$, (ii) in the complementary low latitude region $Nu_{\rm ll} = \langle Nu_{r_o}\rangle_{|\varphi|<|\varphi_{\rm tc}|}$, and (iii) globally over the entire sphere $\langle Nu_{r_o}\rangle_{\varphi}$. In this way, we can demonstrate that the heat transport in the polar region $Nu_{\rm tc}$ shows the typical enhancement behavior of planar RRBC (Fig. 3(a), red triangles). Together with the results above (Fig. 2), it becomes clear that the basic mechanisms, which cause the polar enhancement, remain the same, namely: the formation of axially coherent vortical structures bridging the bulk between the hot and the cold source, such that Ekman pumping of relatively hot/cold fluid from the boundary layers can support the heat transport along the axial direction. However, no enhancement is found for the global heat transport of the full Rayleigh-Bénard sphere (Fig. 3(a), gray circles). The enhanced heat transport inside the polar region is globally balanced by the reduced heat transport in the low latitude region (Fig. 3(a), green squares). It seems that the equatorial reduction strengthens as the polar enhancement increases.

The amplitude of polar heat transport enhancement compared to Nu_0 reaches $\approx$ 28% (Fig. 3(a), red triangles), which is comparable with the enhancement observed in planar RRBC (e.g., Zhong et al., 2009; Kunnen et al., 2011; Yang et al., 2020). The polar enhancement is even larger when only a narrower region directly around the poles is considered (see Supporting Information Fig. S1), which emphasizes the additional influence of the tilt between buoyancy and rotation. Despite the absence of a global heat transport enhancement (relative to Nu_0 of the non-rotating system), the spatial large-scale variations of the heat transport are more important in geo- and astrophysical contexts, like the ocean dynamics of the icy moons. A direct comparison of $Nu_{\rm tc}/Nu_{\rm ll}$ yields up to $\approx 50\%$ larger heat transport in the polar region than in the low latitude region at the maximal polar enhancement (Fig. 3(b), full circles). For strong rotation this ratio inverts as convection halts earlier in the tangent cylinder and will again saturate at 1 once the system is fully in rest (Gastine & Aurnou, 2023).

4 Dependence on the Prandtl number

Heat transport enhancement relative to Nu_0 in planar RRBC essentially depends on Pr. No clear enhancement due to rotation is observed for $Pr < 1$ as the thermal boundary layer is always thinner than the kinetic Ekman layer (Stevens et al., 2010; Yang et al., 2020). To validate this Pr dependence, we conducted additional series of DNSs for $Pr = 1$ and 0.7 (see Supporting Information Tab. S3). As expected, the heat transport enhancement Nu/Nu_0 inside the polar tangent cylinder of spherical RRBC vanishes (see Supporting Information Fig. S2(a)). Interestingly, the heat transport in the low-latitude region also decreases with smaller Pr. Therefore, we can still observe some latitudinal enhancement $Nu_{\rm tc}/Nu_{\rm ll} > 1$ for $Pr = 0.7$ (see Supporting Information Fig. S2(b)) without any polar enhancement $Nu/Nu_0 < 1$. This agrees with the results from Soderlund (2019) performed at $Pr = 1$. However, the latitudinal enhancement $Nu_{\rm tc}/Nu_{\rm ll}$ is significantly smaller than for $Pr = 4.38$. Based on this trend, we conclude that, the polar enhancement Nu/Nu_0, which typically intensifies with increasing Pr above unity, will additionally amplify the latitudinal enhancement $Nu_{\rm tc}/Nu_{\rm ll}$. Since Pr also affects the heat transport in the low latitude region,

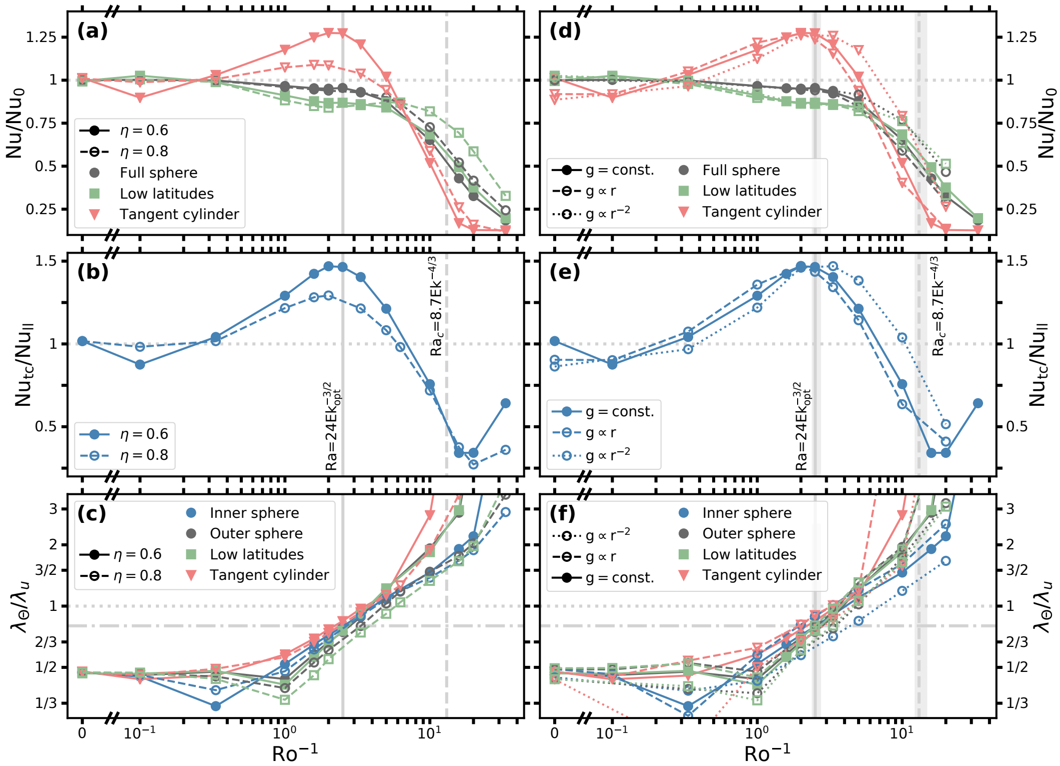

Figure 3. **(a,d)** Heat transport Nu relative to the non-rotating reference Nu_0 as a function of Ro^{-1} for the full sphere ($Nu \equiv \langle Nu_{r_o} \rangle_\varphi$), in the polar region ($Nu_{\mathrm{tc}} = \langle Nu_{r_o} \rangle_{|\varphi|>|\varphi_{\mathrm{tc}}|}$), and in the complementary low latitude region ($Nu_{\mathrm{ll}} = \langle Nu_{r_o} \rangle_{|\varphi|<|\varphi_{\mathrm{tc}}|}$). **(b,e)** Ratio between the heat transport in the polar region Nu_{tc} and the low latitude region Nu_{ll} as a function of Ro^{-1}. **(c,f)** Ratio of thermal and kinetic boundary layer thicknesses λ_Θ/λ_u as a function of Ro^{-1} averaged over the inner sphere, the outer sphere, the polar region, and the low latitude region. **(left)** For different η with constant $g(r) = g_0$, and **(right)** for different $g(r) \propto r^\gamma$ with fixed $\eta = 0.6$. All data at $Pr = 4.38$, $Ra = 10^6$. The solid and dashed vertical lines mark the predicted optimal rotation rate Ro^{-1}_{opt} in planar RRBC given by $Ra = 24Ek^{-3/2}$ (Yang et al., 2020; King et al., 2012) and the predicted onset of convection in planar RRBC given by $Ra_c = 8.7Ek^{-4/3}$ (Chandrasekhar, 1961), respectively. The influence of Ra_{eff} on these transitions (shaded areas) are very limited (see Sec. 6, 7). The dotted and dashed-dotted horizontal lines emphasize ratio 1 and 0.8, respectively.

we speculate that for $Pr \gg 1$, even an enhancement of the global heat transport Nu/Nu_0 is possible.

5 Influence of shell thickness

In fact, the oceans of icy satellites are much thinner water layers, i.e., characterized by a much larger radius ratio than the previous $\eta = 0.6$. For the popular icy satellites indicated in Fig. 1, the estimates are in a range of $0.74 < \eta < 0.99$ (Vance et al., 2018; Soderlund, 2019). A larger η also results in a larger polar tangent cylinder, in which the axial columns connect inner and outer sphere. When we increase the radius ratio to $\eta = 0.8$, the tangent cylinder starts already at $\varphi_{\mathrm{tc}} \approx 36.87$ (compared to $\varphi_{\mathrm{tc}} \approx 53.13$ for $\eta = 0.6$). Interestingly, the heat transport enhancement in the polar tangent cylinder drops to only $\approx 9\%$, whereas the full sphere average remains unchanged throughout the rotation-affected regime (Fig. 3(a), open symbols). This seems very counterintuitive since one would rather expect that a constant enhancement amplitude in the enlarged tangent cylinder, which also affects the global heat transport. We speculate that increasing inclination between radial buoyancy and axial rotation towards the edge of the tangent cylinder reduces the efficiency of vortices pumping heat in the axial direction. However, we note that even at the poles the heat transport enhancement is smaller for $\eta = 0.8$ than for $\eta = 0.6$. (see Supporting Information Fig. S3). Regardless, the heat transport in the polar region can still be significantly larger than at the equator for $\eta = 0.8$, resulting in a latitudinal enhancement up to $\approx 25\%$ (Fig. 3(b), open symbols). The optimal rotation rate Ro_{opt}^{-1} at which the maximal enhancements are achieved, however, remains mostly unaffected.

In the rotation-dominated regime, the heat transport in the polar region decreases similarly with Ro^{-1} for both η. Convection in the tangent cylinder ceases around $Ro_c^{-1} = 8.7^{-3/4} Pr^{1/2} Ra^{1/4} \approx 13.06$ (Fig. 3(a), vertical dashed line), derived from the predicted critical Rayleigh number $Ra_c = 8.7 Ek^{-4/3}$ in planar RRBC (Chandrasekhar, 1961). On the contrary, faster rotation is necessary to suppress convective heat transport in the low latitude region for larger η. Consequently, the equatorial onset of convection in spherical RRBC additionally depends on η, in contrast to Ra_c in planar RRBC valid in the likewise oriented tangent cylinder. Together with the data from Gastine et al. (2016) and Gastine and Aurnou (2023), this reflects that the equatorial onset of convection in spherical RRBC is different than in planar RRBC, i.e., $Ra_{c,sp} = f(\eta, ...)\, Ek^{-4/3}$ rather than $Ra_c = 8.7\, Ek^{-4/3}$.

Lastly, we note the different slopes of the heat transport in the polar and the low latitude region in the rotation-dominated regime. They can be attributed to "steep scaling" $Nu \propto (Ra\, Ek^{4/3})^3 \propto Ro^4$ in the polar region where Ekman puming plays an active role (King et al., 2012, 2013; Julien et al., 2016; Plumley et al., 2016; Gastine & Aurnou, 2023) and (the onset of) "diffusion-free scaling" $Nu \propto (Ra\, Ek^{4/3})^{3/2} \propto Ro^2$ (Gastine et al., 2016; Wang et al., 2021). More detailed evidence for this can be found in the Supporting Information (Text S2, Fig. S4).

6 Sensitivity to different gravity profiles

We further investigate the influence of different radial gravity profiles $g(r) = g_0\ (r/r_o)^\gamma$. Besides a constant gravity ($\gamma = 0$), we apply a homogeneous self-gravitating profile ($\gamma = 1$) and a mass-centered profile ($\gamma = -2$). For this, we stick to $\eta = 0.6$, because the radial gravity variation is larger in thicker shells and so is its expected impact on the heat transport. Aside from minor deviations, we cannot observe major differences in the normalized heat transport Nu/Nu_0 in the rotation-affected regime (until the polar heat transport maximum), including the amplitude of the polar and latitudinal enhancement maxima and their optimal rotation rate Ro_{opt}^{-1} (Fig. 3(d,e)). One might spot a small shift in Ro^{-1} with γ. Its trend likely arises from a change of the effective Rayleigh number of the system $Ra_{\mathrm{eff}} = \langle Ra(r) \rangle_r$, when the gravity varies with r: $Ra_{\mathrm{eff}}(\gamma = 1) < Ra_{\mathrm{eff}}(\gamma = 0) = Ra < Ra_{\mathrm{eff}}(\gamma = -2)$ (see Supporting Information Text S3). Solely in the rotation-dominant regime (beyond the polar heat transport maximum), the heat transport remains considerably larger for smaller γ, i.e., increasing Ra_{eff}. Thus, the relative heat transport enhancement Nu/Nu_0 for $Ro^{-1} \leq Ro^{-1}_{\mathrm{opt}}$ is mostly unaffected by the gravity profile $g(r) = r^{\gamma}$, in contrast to the absolute values Nu (Gastine et al., 2015; Wang et al., 2022). Especially the amplitude of the polar enhancement maximum $Nu_{\max}/Nu_0$ seems to be insensitive to $g(r)$.

7 Relevance of the boundary layer ratio

In planar RRBC, the heat transport maximum for not too large Ra is typically associated with an equal thickness of the thermal and kinetic boundary layers λ_Θ and λ_u (Stevens et al., 2010), which theoretically scales as $\lambda_\Theta/\lambda_u \propto Ek^{3/2}Ra$ (King et al., 2012) giving an estimate for the optimal rotation rate at relatively low Ra (Yang et al., 2020):

$$Ro^{-1}_{\mathrm{opt}} \approx 0.12\, Pr^{1/2} Ra^{1/6} \quad \text{or} \quad Ra \approx 24\, Ek^{-3/2}_{\mathrm{opt}} \ . \tag{6}$$

The predicted Ro^{-1}_{opt} nicely aligns with the heat transport maxima in the polar tangent cylinder independent of η and $g(r)$ (Fig. 3(a,d), solid vertical line). Taking Ra_{eff} into account yields $Ro^{-1}_{\mathrm{opt},\gamma=1} \approx 0.97\, Ro^{-1}_{\mathrm{opt},\gamma=0}$ and $Ro^{-1}_{\mathrm{opt},\gamma=-2} \approx 1.07\, Ro^{-1}_{\mathrm{opt},\gamma=0}$ (see Supporting Information Text S3). Both predicted and observed shifts of Ro^{-1}_{opt} with γ are mostly negligible.

We further verify the predicted boundary layer crossing by directly computing λ_Θ and λ_u from our DNSs as the height of the first peak in the radial profiles of the laterally averaged root-mean-square temperature and lateral velocity, respectively. Due to the asymmetry of cooling and heating in spherical RRBC, the boundary layer thicknesses differ between inner and outer sphere (Gastine et al., 2015). Therefore, we consider λ_Θ and λ_u separately averaged over (i) the inner and (ii) the outer spheres. In addition to the spatial average over the full spheres, we again distinguish between (iii) the polar and (iv) the low latitude regions on the outer sphere. Our data confirms such a typical boundary layer crossing for all the regions (i)-(iv) in the spherical geometry – independent of η (Fig. 3(c)). Furthermore, the polar heat transport maxima and the predicted Ro^{-1}_{opt} perfectly match to an observed boundary layer ratio of $\lambda_\Theta/\lambda_u \approx 0.8$ (dotted horizontal line), especially for the polar region (red symbols) and the inner sphere (blue symbols). This fully agrees with the observations of Yang et al. (2020) in planar RRBC based on the same boundary layer definitions. Only for the thinner $\eta = 0.8$ shell, the boundary layer ratio of the low latitude region (and consequently also for the full outer sphere) lie slightly below the expected $\lambda_\Theta/\lambda_u \approx 0.8$. We also relate this to the different flow orientation at the equator, where the inner and outer shells act more like a sidewall for the axial vortex structures compared to the classical configuration in planar RRBC and the alike tangent cylinder. It therefore is even more remarkable that the boundary layer ratio also matches for the low latitude region in the other cases. For variations of $g(r)$, the agreement with 0.8 is still very good (Fig. 3(f)).

8 Conclusions

Our DNSs of spherical RRBC with Pr larger than unity ($Pr = 4.38$) confirm the main features of heat transport enhancement, as known from planar RRBC, to similarly occur in the spherical geometry:

(i) The three major regimes (buoyancy-dominated, rotation-affected, rotation-dominated) for the heat transport behavior of RRBC can be identified (Kunnen, 2021; Ecke & Shishkina, 2023).

(ii) *Intermediate* rotation enhances the heat transport up to $\approx 28\%$ compared to the non-rotating case inside the polar tangent cylinder, where buoyancy is mostly aligned with the rotation axis and axially coherent vortices (Taylor columns) connect the hot inner with the cold outer shell.

(iii) The maximal (polar) enhancement is determined by an equal thickness of the thermal and kinetic boundary layers $\lambda_\Theta/\lambda_u \approx 1$. The associated optimal rotation rate $Ro_{\rm opt}^{-1} \Leftrightarrow Ek_{\rm opt}^{-1}$ can still be predicted via $Ra \approx 24\,Ek^{-3/2}$ as in planar RRBC (King et al., 2012; Yang et al., 2020).

We however find that the polar heat transport enhancement is accompanied by a reduced heat transport at low latitudes outside the tangent cylinder, where buoyancy is mostly orthogonal to the rotation axis and the axially coherent vortices can only connect both hemispheres of the cold outer shell. The equatorial reduction compensates the polar enhancement on the global average on the one hand, which on the other hand results in an even larger latitudinal enhancement of up to $\approx 50\%$ between the polar and the low latitude region.

We further clarified that the relative heat transport enhancements Nu/Nu_0 and $Nu_{\rm tc}/Nu_{\rm ll}$ are mostly unaffected by the radial gravity profile. Rather surprisingly, a thinner shell ($\eta = 0.8$), which comes along with a larger tangent cylinder, shows less but still significant enhancement ($\approx 9\%$ for Nu/Nu_0 and $\approx 25\%$ for $Nu_{\rm tc}/Nu_{\rm ll}$). The fact that the polar enhancement decreases to remain balanced by the equatorial reduction depicts a non-trivial coupling between the polar and the low latitude region in spherical RRBC.

The existence of polar heat transport enhancement in spherical RRBC, which increases the latitudinal difference between polar and equatorial heat transport, implies that accounting for $Pr > 1$ can be crucial for simulations of icy satellite oceans. Heat transport enhancement on the one hand increases with larger Pr (e.g., Zhong et al., 2009; Stevens et al., 2010) but on the other hand decreases with larger Ra (e.g., Yang et al., 2020). Hence, the question on how much enhancement persists on icy satellites with $Pr > 4.38$ ($10 \lesssim Pr \lesssim 13$) and $Ra \gg 10^6$ ($10^{16} \lesssim Ra \lesssim 10^{24}$) needs to be addressed differently as DNS cannot reach these parameters. However, our findings show, in line with evidences from previous studies (Soderlund, 2019; Amit et al., 2020; Bire et al., 2022), that in principle large Pr related heat transport enhancement could serve as an explanation for latitudinal heat transport and associated ice thickness variations on icy satellites.

Open Research Section

Data availability statement

The data that support the findings of this study are openly available in *4TU.ResearchData* at `http://doi.org/tba_on_publication`.

Acknowledgments

This work was funded by the ERC Starting Grant *UltimateRB* No. 804283. We acknowledge the access to several computational resources, all of which were used for this work: PRACE for awarding us access to MareNostrum4 at the Barcelona Supercomputing Center (BSC), Spain and IRENE at Très Grand Centre de Calcul (TGCC) du CEA, France (project 2021250115), and EuroHPC for awarding us access to Discoverer at Sofiatech, Bulgaria (No. EHPC-REG-2022R03-208).

References

Aguirre Guzmán, A. J., Madonia, M., Cheng, J. S., Ostilla-Mónico, R., Clercx, H. J., & Kunnen, R. P. (2020). Competition between Ekman Plumes and Vortex Condensates in Rapidly Rotating Thermal Convection. *Phys. Rev. Lett.*, *125*, 214501.

Ahlers, G., Grossmann, S., & Lohse, D. (2009). Heat transfer and large scale dynamics in turbulent Rayleigh-Bénard convection. *Rev. Mod. Phys.*, *81*, 503–537.

Amit, H., Choblet, G., Tobie, G., Terra-Nova, F., Čadek, O., & Bouffard, M. (2020). Cooling patterns in rotating thin spherical shells — Application to Titan's subsurface ocean. *ICARUS*, *338*, 113509.

Aurnou, J., Calkins, M., Cheng, J., Julien, K., King, E., Nieves, D., ... Stellmach, S. (2015). Rotating convective turbulence in Earth and planetary cores. *Phys. Earth Planet. Inter.*, *246*, 52–71.

Beuthe, M., Rivoldini, A., & Trinh, A. (2016). Enceladus's and Dione's floating ice shells supported by minimum stress isostasy. *Geophys. Res. Lett.*, *43*(19), 10,088–10,096.

Bire, S., Kang, W., Ramadhan, A., Campin, J., & Marshall, J. (2022). Exploring Ocean Circulation on Icy Moons Heated From Below. *J. Geophys. Res. Planets*, *127*(3).

Busse, F. H. (1970). Thermal instabilities in rapidly rotating systems. *J. Fluid Mech.*, *44*(3), 441–460.

Busse, F. H. (1983). A model of mean zonal flows in the major planets. *Geophys. Astrophys. Fluid Dyn.*, *23*(2), 153–174.

Chandrasekhar, S. (1961). *Hydrodynamic and hydromagnetic stability.* Oxford University Press.

Cheng, J. S., Stellmach, S., Ribeiro, A., Grannan, A., King, E. M., & Aurnou, J. M. (2015). Laboratory-numerical models of rapidly rotating convection in planetary cores. *Geophys. J. Int.*, *201*, 1–17.

Chyba, C. F., & Hand, K. P. (2005). Astrobiology: The Study of the Living Universe. *Annu. Rev. Astron. Astrophys.*, *43*(1), 31–74.

Ecke, R. E., & Niemela, J. J. (2014). Heat Transport in the Geostrophic Regime of Rotating Rayleigh-Bénard Convection. *Phys. Rev. Lett.*, *113*, 114301.

Ecke, R. E., & Shishkina, O. (2023). Turbulent Rotating Rayleigh-Bénard Convection. *Annu. Rev. Fluid Mech.*, *55*, 603-38.

Gastine, T., & Aurnou, J. M. (2023). Latitudinal regionalization of rotating spherical shell convection. *J. Fluid Mech.*, *954*, R1.

Gastine, T., Wicht, J., & Aubert, J. (2016). Scaling regimes in spherical shell rotating convection. *J. Fluid Mech.*, *808*, 690–732.

Gastine, T., Wicht, J., & Aurnou, J. M. (2015). Turbulent Rayleigh–Bénard convection in spherical shells. *J. Fluid Mech.*, *778*, 721–764.

Hemingway, D. J., & Mittal, T. (2019). Enceladus's ice shell structure as a window on internal heat production. *ICARUS*, *332*, 111–131.

Julien, K., Aurnou, J. M., Calkins, M. A., Knobloch, E., Marti, P., Stellmach, S., & Vasil, G. M. (2016). A nonlinear model for rotationally constrained convection with Ekman pumping. *J. Fluid Mech.*, *798*, 50–87.

Julien, K., Knobloch, E., Rubio, A. M., & Vasil, G. M. (2012). Heat transport in low-Rossby-number Rayleigh-Bénard convection. *Phys. Rev. Lett.*, *109*(25), 254503.

Julien, K., Legg, S., McWilliams, J., & Werne, J. (1996). Rapidly rotating Rayleigh-Bénard convection. *J. Fluid Mech.*, *322*, 243–273.

Julien, K., Rubio, A., Grooms, I., & Knobloch, E. (2012). Statistical and physical balances in low Rossby number Rayleigh-Bénard convection. *Geophys. Astrophys. Fluid Dyn.*, *106*, 392–428.

Kang, W. (2022). Different Ice-shell Geometries on Europa and Enceladus due to Their Different Sizes: Impacts of Ocean Heat Transport. *Astrophys. J.*, *934*(2), 116.

Kang, W., & Jansen, M. (2022). On Icy Ocean Worlds, Size Controls Ice Shell Geometry. *Astrophys. J.*, *935*(2), 103.

Kihoulou, M., Čadek, O., Kvorka, J., Kalousová, K., Choblet, G., & Tobie, G. (2023). Topographic response to ocean heat flux anomaly on the icy moons of Jupiter and Saturn. *ICARUS*, *391*, 115337.

King, E. M., Stellmach, S., & Aurnou, J. M. (2012). Heat transfer by rapidly rotating Rayleigh-Bénard convection. *J. Fluid Mech.*, *691*, 568–582.

King, E. M., Stellmach, S., & Buffett, B. (2013). Scaling behaviour in Rayleigh-Bénard convection with and without rotation. *J. Fluid Mech.*, *717*, 449–471.

Kunnen, R. P. J. (2021). The geostrophic regime of rapidly rotating turbulent convection. *J. Turbul.*, *22*, 267-296.

Kunnen, R. P. J., Clercx, H. J. H., & Geurts, B. J. (2006). Heat flux intensification by vortical flow localization in rotating convection. *Phys. Rev. E*, *74*, 056306.

Kunnen, R. P. J., Stevens, R. J. A. M., Overkamp, J., Sun, C., Heijst, G. J. F. v., & Clercx, H. J. H. (2011). The role of Stewartson and Ekman layers in turbulent rotating Rayleigh-Bénard convection. *J. Fluid Mech.*, *688*, 422–442.

Nimmo, F., & Pappalardo, R. T. (2016). Ocean worlds in the outer solar system. *J. Geophys. Res. Planets*, *121*(8), 1378–1399.

Plumley, M., & Julien, K. (2019). Scaling Laws in Rayleigh-Bénard Convection. *Earth Space Sci.*, *6*(9), 1580–1592.

Plumley, M., Julien, K., Marti, P., & Stellmach, S. (2016). The effects of Ekman pumping on quasi-geostrophic Rayleigh-Bénard convection. *J. Fluid Mech.*, *803*, 51–71.

Proudman, J. (1916). On the motion of solids in a liquid possessing vorticity. *Proc. R. Soc. London A*, *92*, 408–424.

Roberts, P. H. (1968). On the thermal instability of a rotating-fluid sphere containing heat sources. *Philos. Trans. R. Soc. A*, *263*(1136), 93–117.

Rossby, H. T. (1969). A study of Bénard convection with and without rotation. *J. Fluid Mech.*, *36*, 309–335.

Santelli, L., Orlandi, P., & Verzicco, R. (2020). A finite-difference scheme for three-dimensional incompressible flows in spherical coordinates. *J. Comput. Phys.*, *424*, 109848.

Shishkina, O., Stevens, R. J. A. M., Grossmann, S., & Lohse, D. (2010). Boundary layer structure in turbulent thermal convection and its consequences for the required numerical resolution. *New J. Phys.*, *12*, 075022.

Soderlund, K. M. (2019). Ocean Dynamics of Outer Solar System Satellites. *Geophys. Res. Lett.*, *46*, 8700–8710.

Soderlund, K. M., King, E. M., & Aurnou, J. M. (2012). The influence of magnetic fields in planetary dynamo models. *Earth Planet. Sci. Lett.*, *333-334*, 9–20.

Sprague, M., Julien, K., Knobloch, E., & Werne, J. (2006). Numerical simulation of an asymptotically reduced system for rotationally constrained convection. *J. Fluid Mech.*, *551*, 141–174.

Stellmach, S., Lischper, M., Julien, K., Vasil, G., Cheng, J. S., Ribeiro, A., … Aurnou, J. M. (2014). Approaching the Asymptotic Regime of Rapidly Rotating Convection: Boundary Layers versus Interior Dynamics. *Phys. Rev. Lett.*, *113*, 254501.

Stevens, R. J. A. M., Blass, A., Zhu, X., Verzicco, R., & Lohse, D. (2018). Turbulent thermal superstructures in Rayleigh-Bénard convection. *Phys. Rev. Fluids*, *3*, 041501(R).

Stevens, R. J. A. M., Clercx, H. J. H., & Lohse, D. (2010). Optimal Prandtl number for heat transfer in rotating Rayleigh-Bénard convection. *New J. Phys.*, *12*, 075005.

Stevens, R. J. A. M., Clercx, H. J. H., & Lohse, D. (2013). Heat transport and flow structure in rotating Rayleigh-Bénard convection. *Eur. J. Mech. B/Fluids*, *40*, 41–49.

Stevens, R. J. A. M., Zhong, J.-Q., Clercx, H. J. H., Ahlers, G., & Lohse, D. (2009). Transitions between turbulent states in rotating Rayleigh-Bénard convection. *Phys. Rev. Lett.*, *103*, 024503.

Taylor, G. I. (1917). Motion of solids in fluids when the flow is not irrotational. *Proc. R. Soc. London A*, *93*(648), 99-113.

Taylor, G. I. (1923). Stability of a viscous liquid contained between two rotating cylinders. *Phil. Trans. R. Soc. A*, *223*, 289–343.

Vance, S. D., Panning, M. P., Stähler, S., Cammarano, F., Bills, B. G., Tobie, G., … Banerdt, B. (2018). Geophysical Investigations of Habitability in Ice-Covered Ocean Worlds. *J. Geophys. Res. Planets*, *123*(1), 180–205.

van der Poel, E. P., Stevens, R. J. A. M., & Lohse, D. (2013). Comparison between two and three dimensional Rayleigh-Bénard convection. *J. Fluid Mech.*, *736*, 177–194.

Wang, G., Santelli, L., Lohse, D., Verzicco, R., & Stevens, R. J. A. M. (2021). Diffusion-free scaling in rotating spherical Rayleigh-Bénard convection. *Geophys. Res. Lett.*, *48*(20), e2021GL095017.

Wang, G., Santelli, L., Verzicco, R., Lohse, D., & Stevens, R. J. A. M. (2022). Off-centre gravity induces large-scale flow patterns in spherical Rayleigh–Bénard convection. *J. Fluid Mech.*, *942*, A21.

Weiss, S., Stevens, R. J. A. M., Zhong, J.-Q., Clercx, H. J. H., Lohse, D., & Ahlers, G. (2010). Finite-size effects lead to supercritical bifurcations in turbulent rotating Rayleigh-Bénard convection. *Phys. Rev. Lett.*, *105*, 224501.

Weiss, S., Wei, P., & Ahlers, G. (2016). Heat-transport enhancement in rotating turbulent Rayleigh-Bénard convection. *Phys. Rev. E*, *93*, 043102.

Yang, Y., Verzicco, R., Lohse, D., & Stevens, R. J. A. M. (2020). What rotation rate maximizes heat transport in rotating Rayleigh-Bénard convection with Prandtl number larger than one? *Phys. Rev. Fluids*, *5*(5), 053501.

Zhong, J.-Q., Stevens, R. J. A. M., Clercx, H. J. H., Verzicco, R., Lohse, D., & Ahlers, G. (2009). Prandtl-, Rayleigh-, and Rossby-number dependence of heat transport in turbulent rotating Rayleigh-Bénard convection. *Phys. Rev. Lett.*, *102*, 044502.

Čadek, O., Souček, O., Běhounková, M., Choblet, G., Tobie, G., & Hron, J. (2019). Long-term stability of Enceladus' uneven ice shell. *ICARUS*, *319*, 476–484.

Supporting Information for ”Towards understanding polar heat transport enhancement in sub-glacial oceans on icy moons”

Robert Hartmann[1], Richard J.A.M. Stevens[1], Detlef Lohse[1,2], and Roberto Verzicco[1,3,4]

[1]Physics of Fluids Group and Twente Max Planck Center, J.M. Burgers Center for Fluid Dynamics,

University of Twente, 7500 AE Enschede, The Netherlands

[2]Max Planck Institute for Dynamics and Self-Organisation, 37077 Göttingen, Germany

[3]Dipartimento di Ingegneria Industriale, University of Rome ’Tor Vergata’, 00133 Rome, Italy

[4]Gran Sasso Science Institute, 67100 L’Aquila, Italy

Contents of this file

Introduction

Further details of the direct numerical simulations (DNSs) of rotating Rayleigh-Bénard convection (RRBC) in the spherical geometry (controlled by the dimensionless Prandtl number Pr, Rayleigh number Ra, and Rossby (or Ekman) number Ro (Ek), see main letter for full definitions) are provided in this file.

Text S1: Numerical Details

The DNSs use a central second-order accurate finite-difference scheme on a staggered grid in spherical coordinates (Santelli et al., 2020). The code, specialized for Rayleigh-Bénard systems, has been adopted to account for constant rotation around its central polar axis in the limit of a rotational Froude number $Fr = 0$, i.e., accounting for Coriolis forcing but neglecting the effect of centrifugal forcing on buoyancy (Wang et al., 2021). The limit of $Fr \to 0$ is valid in most geo- and astrophysical contexts (e.g., $Fr_{\text{Earth}} \approx 8.7 \cdot 10^{-5}$). All DNSs simulate a full spherical shell, i.e., no symmetric folding is applied along the Longitude ϑ, to not affect the dynamics across the polar axis in the buoyancy-dominated and rotation-affected regimes by enforcing a fully symmetric behavior around the polar axis.

All DNSs are performed at $Ra = 10^6$. The number of grid points in radial direction varies between $N_r = 72$ for constant $g(r) = g_0$ and $N_r = 108$ for $g(r) \propto r^{-2}$. A clipped Chebyshev-like clustering of grid points towards the plates is applied in the radial direction to ensure a sufficient resolution of the plate boundary layers. The resolution of the thermal/kinetic boundary layers strictly follows (Shishkina et al., 2010):

$$N_{BL,\Theta} \gtrsim 0.47 \cdot \sqrt{2 \cdot Nu_{\text{est}}} \tag{1}$$

$$N_{BL,u} \gtrsim 0.48 \cdot \sqrt{2 \cdot Nu_{\text{est}}} \cdot Pr^{1/3} \tag{2}$$

Here, $N_{BL,\{\Theta,u\}}$ is the number of grid points in the boundary layer and Nu_{est} a *a priori* estimate of the Nusselt number. The spatial directions are uniformly spaced in angle φ and ϑ, accounting for their maximal spacing at equator of the outer sphere. The dynamic time stepping in our DNSs is controlled by a maximum CFL number (1.1) and a maximum time step ($5 \cdot 10^{-3}$ free-fall time units). The numerical parameters of the DNSs are summarized Tabs. S1-S3. All DNSs are run very long such that integral flow properties (like the Nusselt number Nu) are converged within a tolerance of 0.5%.

Text S2: Heat transport scaling at rapid rotation

The heat transport in rapidly rotating Rayleigh-Bénard convection (with $Ek \to 0$) is found to scale with the supercriticality of the system (King et al., 2012; Julien et al., 2012; Stellmach et al., 2014; Cheng et al., 2015):

$$Nu \propto \left(Ra\, Ek^{4/3}\right)^{\alpha} \tag{3}$$

In the canonical RRBC in planar configuration with no-slip boundaries, $\alpha = 3$ is predicted for $Ra \lesssim Ek^{-3/2}$ (King et al., 2012, 2013). On the contrary, $\alpha = 3/2$ is predicted in the asymptotic limit without molecular diffusion, which is known as *diffusion-free scaling*. Diffusion-free scaling in planar RRBC is only found for free-slip boundary conditions and small $Ek \lesssim 10^{-6}$ (Stellmach et al., 2014; Kunnen et al., 2016; Wang et al., 2021) or in asymptotically reduced models (Julien et al., 2012). The difference between $\alpha = 3$ and $\alpha = 3/2$ is attributed to the active role of Ekman pumping for no-slip boundaries (Stellmach et al., 2014; Julien et al., 2016; Plumley et al., 2016).

However, both scaling types are reported for spherical RRBC. Inside the polar tangent cylinder, i.e, the cylinder aligned with the polar axis and radius r_i of the inner sphere, an exponent $\alpha = 3$ is found (Wang et al., 2021; Gastine & Aurnou, 2023), whereas $\alpha = 3/2$

is observed at low latitudes outside the tangent cylinder (Gastine et al., 2016; Wang et al., 2021).

From Eq. 4 follows that, for fixed Pr and Ra, the heat transport in the rotation-dominated regime (if approaching the quasi-geostrophic state) should follow:

$$Nu \propto Ro^{\frac{4}{3}\alpha} = \begin{cases} Ro^4 & : \alpha = 3 \\ Ro^2 & : \alpha = 3/2 \end{cases} \tag{4}$$

Although our simulations do not reach to small $Ek < 10^{-6}$, we observe considerable different scaling behavior for the heat transport inside and outside the tangent cylinder, which almost meet the scaling exponents 4 and 2 predicted by Eq. 4 (see Fig. S4).

Text S3: Influence of the gravity profile on the effective Rayleigh number

The definition of the classical Rayleigh number Ra does only account for a constant gravitational acceleration g_0. Whenever the actual gravitational acceleration g varies locally, the effective Rayleigh number Ra_{eff}, i.e., the volume averaged local Rayleigh number of the system, differs from Ra. In our case the reference Ra is defined as:

$$Ra = \frac{\alpha g_0 \Delta T H^3}{\nu \kappa} \ , \tag{5}$$

where g_0 is the reference gravitational acceleration at the outer sphere (ν, κ, α, ΔT, and H are the kinematic viscosity, the thermal diffusivity, the isobaric thermal expansion coefficient, the temperature difference between inner and outer sphere, and the shell thickness, respectively). For any gravity profile $g(r) = g_0\,(r/r_o)^\gamma$ with $\gamma \neq 0$, the effective Rayleigh number changes depending on γ:

$$Ra_{\text{eff}} \equiv \left\langle \frac{\alpha g(r) \Delta T H^3}{\nu\kappa} \right\rangle_V = Ra \left\langle \left(\frac{r}{r_o}\right)^\gamma \right\rangle_V = Ra \, \frac{3}{(r_o^3 - r_i^3)} \int\limits_{r_i}^{r_o} \left(\frac{r}{r_o}\right)^\gamma r^2 \mathrm{d}r \ , \tag{6}$$

where r_i and r_o are the radii of inner and outer sphere and $\langle\cdot\rangle_V$ denotes the volume average over the full shell. Solving the integral for $\gamma = 1$, 0, and -2 and $\eta = r_i/r_o = 0.6$ yields:

$$Ra_{\text{eff}} = \begin{cases} Ra \, \frac{3\eta}{1+\eta+\eta^2+\eta^3} \approx 0.83 \, Ra & : \gamma = 1 \\ Ra & : \gamma = 0 \\ Ra \, \frac{3}{1+\eta+\eta^2} \approx 1.53 \, Ra & : \gamma = -2 \end{cases} \tag{7}$$

Considering Ra_{eff} in the estimates for the optimal rotation rate $Ro^{-1}_{\text{opt}} \propto Ra_{\text{eff}}^{1/6}$ and the onset of convection $Ro_c^{-1} \propto Ra_{\text{eff}}^{1/4}$ then yields

$$Ro^{-1}_{\text{opt},\gamma} \approx \begin{cases} 0.83^{1/6} \, Ro^{-1}_{\text{opt},\gamma=0} \approx 0.97 \, Ro^{-1}_{\text{opt},\gamma=0} & : \gamma = 1 \\ 1.53^{1/6} \, Ro^{-1}_{\text{opt},\gamma=0} \approx 1.07 \, Ro^{-1}_{\text{opt},\gamma=0} & : \gamma = -2 \end{cases} \tag{8}$$

and

$$Ro^{-1}_{c,\gamma} \approx \begin{cases} 0.83^{1/4} \, Ro^{-1}_{c,\gamma=0} \approx 0.95 \, Ro^{-1}_{c,\gamma=0} & : \gamma = 1 \\ 1.53^{1/4} \, Ro^{-1}_{c,\gamma=0} \approx 1.11 \, Ro^{-1}_{c,\gamma=0} & : \gamma = -2 \end{cases} \tag{9}$$

This can help to explain the observed minimal trend in the shift of Ro^{-1}_{opt} (and likewise Ro_c^{-1}) in the tangent cylinder for the different γ (main letter Fig. 3).

References

Cheng, J. S., Stellmach, S., Ribeiro, A., Grannan, A., King, E. M., & Aurnou, J. M. (2015). Laboratory-numerical models of rapidly rotating convection in planetary cores. *Geophys. J. Int.*, *201*, 1–17.

Gastine, T., & Aurnou, J. M. (2023). Latitudinal regionalization of rotating spherical shell convection. *J. Fluid Mech.*, *954*, R1.

Gastine, T., Wicht, J., & Aubert, J. (2016). Scaling regimes in spherical shell rotating convection. *J. Fluid Mech.*, *808*, 690–732.

Julien, K., Aurnou, J. M., Calkins, M. A., Knobloch, E., Marti, P., Stellmach, S., & Vasil, G. M. (2016). A nonlinear model for rotationally constrained convection with Ekman pumping. *J. Fluid Mech.*, *798*, 50–87.

Julien, K., Knobloch, E., Rubio, A. M., & Vasil, G. M. (2012). Heat transport in low-Rossby-number Rayleigh-Bénard convection. *Phys. Rev. Lett.*, *109*(25), 254503.

King, E. M., Stellmach, S., & Aurnou, J. M. (2012). Heat transfer by rapidly rotating Rayleigh-Bénard convection. *J. Fluid Mech.*, *691*, 568–582.

King, E. M., Stellmach, S., & Buffett, B. (2013). Scaling behaviour in Rayleigh-Bénard convection with and without rotation. *J. Fluid Mech.*, *717*, 449–471.

Kunnen, R. P. J., Ostilla-Mónico, R., Poel, E. P. v. d., Verzicco, R., & Lohse, D. (2016). Transition to geostrophic convection: The role of the boundary conditions. *J. Fluid Mech.*, *799*, 413–432.

Plumley, M., Julien, K., Marti, P., & Stellmach, S. (2016). The effects of Ekman pumping on quasi-geostrophic Rayleigh-Bénard convection. *J. Fluid Mech.*, *803*, 51–71.

Santelli, L., Orlandi, P., & Verzicco, R. (2020). A finite-difference scheme for three-dimensional incompressible flows in spherical coordinates. *J. Comput. Phys.*, *424*, 109848.

Shishkina, O., Stevens, R. J. A. M., Grossmann, S., & Lohse, D. (2010). Boundary layer structure in turbulent thermal convection and its consequences for the required numerical resolution. *New J. Phys.*, *12*, 075022.

Stellmach, S., Lischper, M., Julien, K., Vasil, G., Cheng, J. S., Ribeiro, A., ... Aurnou, J. M. (2014). Approaching the Asymptotic Regime of Rapidly Rotating Convection:

Boundary Layers versus Interior Dynamics. *Phys. Rev. Lett.*, *113*, 254501.

Wang, G., Santelli, L., Lohse, D., Verzicco, R., & Stevens, R. J. A. M. (2021). Diffusion-free scaling in rotating spherical Rayleigh-Bénard convection. *Geophys. Res. Lett.*, *48*(20), e2021GL095017.

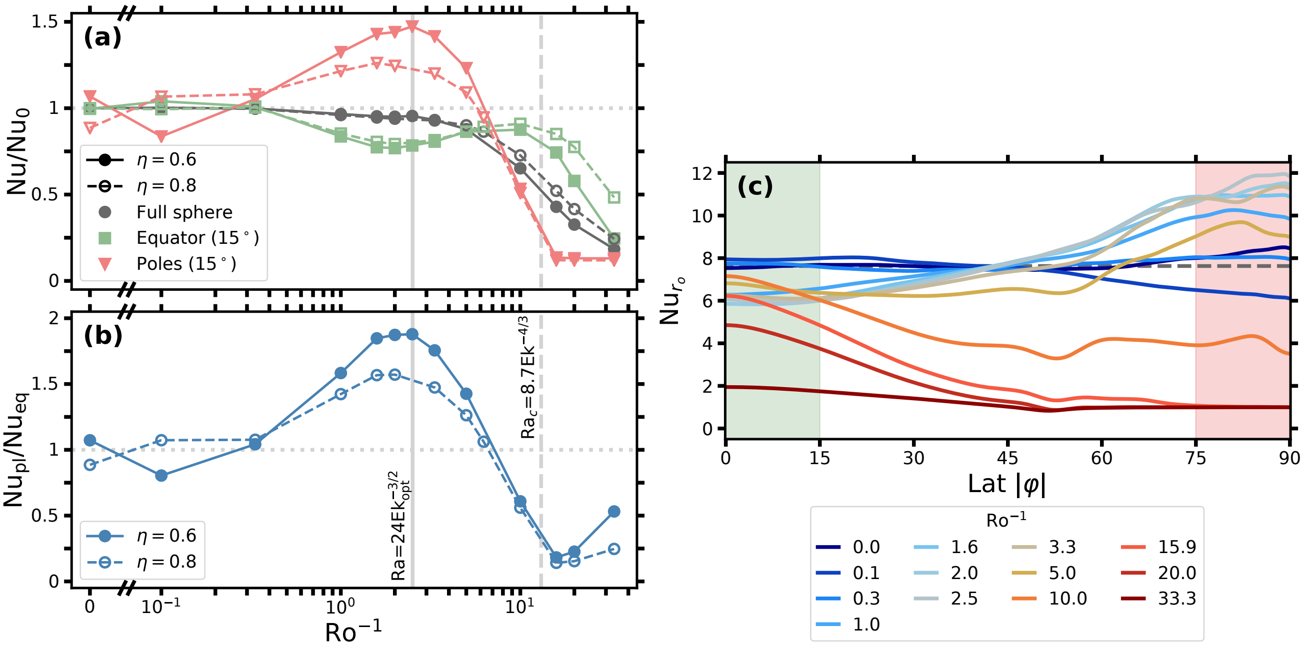

Figure S1. **(a)** Heat transport Nu relative to the non-rotating reference Nu_0 as a function of Ro^{-1} for different η with constant $g(r) = g_0$, $Pr = 4.38$, $Ra = 10^6$ averaged over the full sphere ($Nu \equiv \langle Nu_{r_o} \rangle_\varphi$), in 15° around the pole ($Nu_{\mathrm{pl}} = \langle Nu_{r_o} \rangle_{|\varphi|>75^\circ}$), and in 15° around the equator ($Nu_{\mathrm{eq}} = \langle Nu_{r_o} \rangle_{|\varphi|<15^\circ}$). **(b)** Ratio between the polar heat transport Nu_{pl} and the equatorial heat transport Nu_{eq} as a function of Ro^{-1}. **(c)** Dimensionless heat transport at the outer sphere Nu_{r_o} as function of the latitude $|\varphi|$ for various rotation rates Ro^{-1} with $Ra = 10^6$, $Pr = 4.38$, $\eta = 0.6$ and $g(r) = g_0$, where the color shaded regions illustrate the limited averaging.

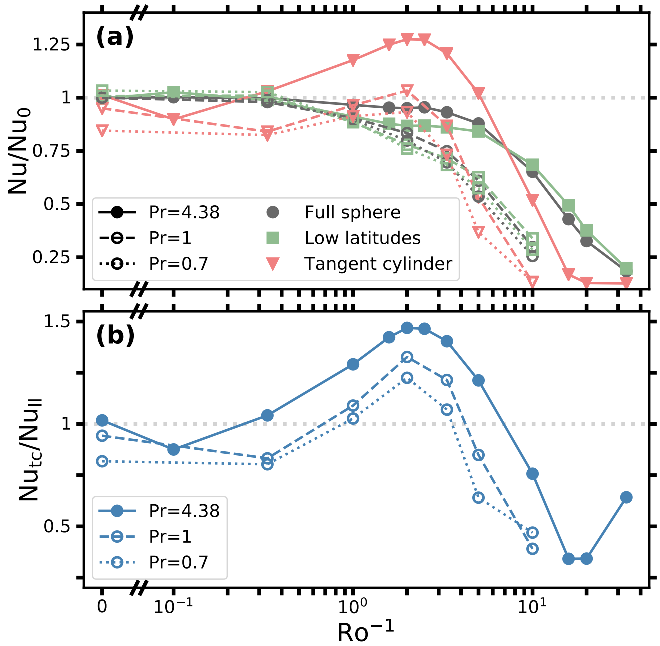

Figure S2. **(a)** Heat transport Nu relative to the non-rotating reference Nu_0 for the full sphere ($Nu \equiv \langle Nu_{r_o} \rangle_\varphi$), in the polar region ($Nu_{\rm tc} = \langle Nu_{r_o} \rangle_{|\varphi|>|\varphi_{\rm tc}|}$), and in the complementary low latitude region ($Nu_{\rm ll} = \langle Nu_{r_o} \rangle_{|\varphi|<|\varphi_{\rm tc}|}$), and **(b)** ratio between the heat transport in the polar region $Nu_{\rm tc}$ and the low latitude region $Nu_{\rm ll}$ as a functions of Ro^{-1} for different Pr with constant $g(r) = g_0$, $\eta = 0.6$, $Ra = 10^6$.

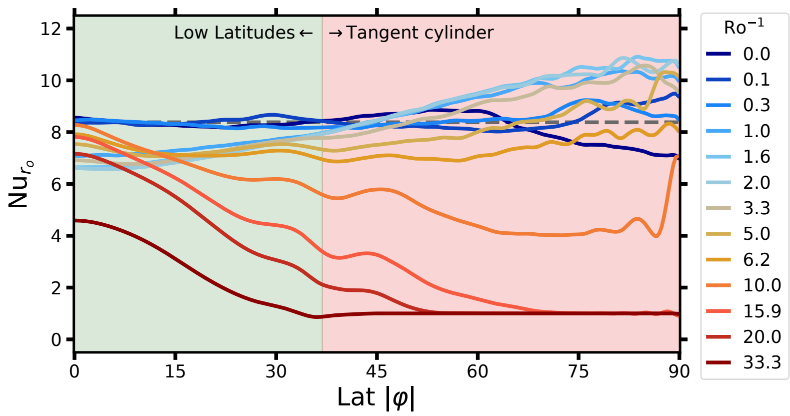

Figure S3. Dimensionless heat transport at the outer sphere Nu_{r_o} as function of the latitude $|\varphi|$ for various rotation rates Ro^{-1} at $Ra = 10^6$ and $Pr = 4.38$ with $\eta = 0.8$ and constant $g(r) = g_0$.

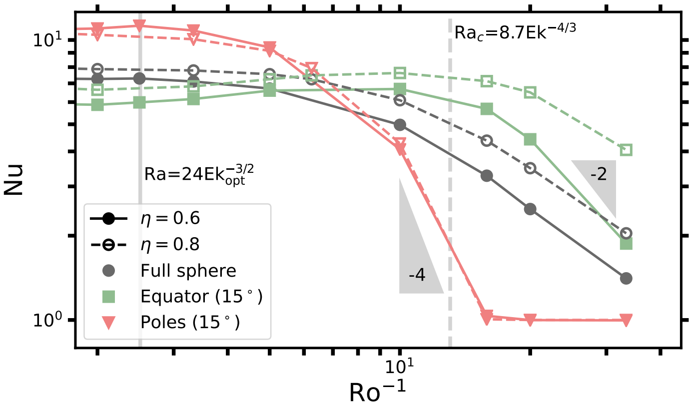

Figure S4. Heat transport Nu as a function of Ro^{-1} for $\eta = 0.6$ and 0.8 with constant $g(r) = g_0$, $Pr = 4.38$, $Ra = 10^6$ averaged over the full sphere, in 15° around the pole, and in 15° around the equator. Zoomed view on the rotation-dominated regime and the onset of convection highlighting the different effective scalings of the heat transport inside and outside the polar tangent cylinder.

Table S1. Summary of numerical parameters for the DNSs, all at $Pr = 4.38$ and $Ra = 10^6$, for $\gamma = 0$: radius ratio η; gravity exponent γ; inverse Rossby number Ro^{-1}; number of grid points in radial, latitudinal and longitudinal directions N_r, N_φ, N_ϑ; averaging interval $\Delta t_{\rm avg}$ in units of free-fall time; Nusselt number Nu averaged over the entire $\delta t_{\rm avg}$; Nusselt number Nu_h averaged over the 2nd half of $\delta t_{\rm avg}$; Nusselt number inside and outside the polar tangent cylinder $Nu_{\rm tc}$ and $Nu_{\rm ll}$, respectively.

η	γ	Ro^{-1}	N_r	N_φ	N_ϑ	$\Delta t_{\rm avg}$	Nu	Nu_h	$Nu_{\rm tc}$	$Nu_{\rm ll}$
0.6	0	0	72	384	768	900	7.634	7.633	7.729	7.596
0.6	0	0.1	72	384	768	900	7.651	7.643	6.856	7.831
0.6	0	$0.\bar{3}$	72	384	768	900	7.620	7.617	7.864	7.548
0.6	0	1	72	384	768	889	7.376	7.377	8.983	6.958
0.6	0	1.6	72	384	768	900	7.276	7.274	9.534	6.699
0.6	0	2	72	384	768	900	7.275	7.259	9.731	6.624
0.6	0	2.5	80	384	768	900	7.289	7.289	9.716	6.633
0.6	0	$3.\bar{3}$	72	384	768	900	7.110	7.116	9.222	6.569
0.6	0	5	72	384	768	900	6.709	6.715	7.789	6.423
0.6	0	10	72	384	768	900	4.977	4.960	3.959	5.228
0.6	0	15.9	72	384	768	900	3.275	3.282	1.289	3.770
0.6	0	20	72	384	768	900	2.490	2.480	0.984	2.872
0.6	0	$33.\bar{3}$	72	384	768	900	1.408	1.407	0.968	1.508
0.8	0	0	72	512	1024	500	8.380	8.376	8.458	8.316
0.8	0	0.1	72	512	1024	500	8.371	8.385	8.276	8.422
0.8	0	$0.\bar{3}$	72	512	1024	496	8.355	8.358	8.434	8.294
0.8	0	1	72	512	1024	500	8.047	8.044	9.003	7.401
0.8	0	1.6	72	512	1024	500	7.927	7.922	9.127	7.121
0.8	0	2	72	512	1024	500	7.870	7.863	9.101	7.041
0.8	0	$3.\bar{3}$	72	512	1024	500	7.784	7.786	8.700	7.165
0.8	0	5	72	512	1024	500	7.550	7.554	7.905	7.301
0.8	0	6.25	72	512	1024	597	7.240	7.239	7.155	7.292
0.8	0	10	72	512	1024	500	6.093	6.100	4.931	6.863
0.8	0	15.9	72	512	1024	900	4.370	4.369	2.187	5.815
0.8	0	20	72	512	1024	900	3.485	3.475	1.338	4.912
0.8	0	$33.\bar{3}$	72	512	1024	900	2.040	2.042	0.989	2.743

Table S2. Summary of numerical parameters for the DNSs, all at $Pr = 4.38$ and $Ra = 10^6$, for $\gamma \neq 0$ (columns as in Tab. S1).

η	γ	Ro^{-1}	N_r	N_φ	N_ϑ	Δt_{avg}	Nu	Nu_h	Nu_{tc}	Nu_{ll}
0.6	1	0	80	384	768	600	6.988	6.981	6.423	7.103
0.6	1	0.1	80	384	768	600	7.001	7.007	6.416	7.113
0.6	1	$0.\bar{3}$	80	384	768	600	6.961	6.952	7.342	6.833
0.6	1	1	80	384	768	600	6.745	6.744	8.515	6.269
0.6	1	2	80	384	768	600	6.637	6.642	8.883	6.040
0.6	1	2.5	80	384	768	600	6.578	6.571	8.653	6.027
0.6	1	$3.\bar{3}$	80	384	768	597	6.450	6.436	8.070	6.010
0.6	1	5	80	384	768	1000	5.921	5.929	6.555	5.734
0.6	1	10	80	384	768	1000	4.124	4.131	2.817	4.430
0.6	1	20	80	384	768	985	2.040	2.042	0.951	2.361
0.6	-2	0	108	432	864	489	9.318	9.320	8.256	9.559
0.6	-2	$0.\bar{3}$	108	432	864	592	9.253	9.240	8.996	9.291
0.6	-2	1	108	432	864	591	8.984	8.998	10.475	8.589
0.6	-2	2	108	432	864	554	8.799	8.784	11.749	8.044
0.6	-2	$3.\bar{3}$	108	432	864	578	8.737	8.747	11.723	7.976
0.6	-2	5	108	432	864	535	8.538	8.548	10.948	7.918
0.6	-2	10	108	432	864	756	7.170	7.159	7.379	7.101
0.6	-2	20	108	432	864	1047	4.346	4.356	2.469	4.791

Table S3. Summary of numerical parameters for the DNSs for $Pr \neq 4.38$, $Ra = 10^6$, $\eta = 0.6$, $\gamma = 0$ (columns as in Tab. S1 with Pr instead of η and γ).

Pr	Ro^{-1}	N_r	N_φ	N_ϑ	Δt_{avg}	Nu	Nu_h	Nu_{tc}	Nu_{ll}
1	0	72	384	768	665	7.507	7.507	7.132	7.566
1	$0.\bar{3}$	72	384	768	377	7.352	7.333	6.308	7.580
1	1	72	384	768	600	6.786	6.810	7.238	6.641
1	2	72	384	768	600	6.259	6.256	7.758	5.846
1	$3.\bar{3}$	72	384	768	600	5.611	5.611	6.517	5.365
1	5	72	384	768	600	4.576	4.571	3.990	4.701
1	10	72	384	768	1000	2.237	2.233	0.993	2.544
0.7	0	72	384	768	114	7.335	7.34	6.200	7.579
0.7	$0.\bar{3}$	72	384	768	286	7.256	7.242	6.046	7.528
0.7	1	72	384	768	600	6.582	6.578	6.697	6.523
0.7	2	72	384	768	600	5.857	5.855	6.838	5.581
0.7	$3.\bar{3}$	72	384	768	600	5.104	5.107	5.365	5.014
0.7	5	72	384	768	1000	3.925	3.934	2.699	4.215
0.7	10	72	384	768	1000	1.876	1.876	0.984	2.096